Monthly Notices
of the
ROYAL ASTRONOMICAL SOCIETY

MNRAS **464,** 3369–3384 (2017)
Advance Access publication 2016 October 13

doi:10.1093/mnras/stw2630

The SCUBA-2 Cosmology Legacy Survey: the EGS deep field – I. Deep number counts and the redshift distribution of the recovered cosmic infrared background at 450 and 850 μm

J. A. Zavala,[1⋆] I. Aretxaga,[1] J. E. Geach,[2] D. H. Hughes,[1] M. Birkinshaw,[3] E. Chapin,[4] S. Chapman,[5] Chian-Chou Chen,[6] D. L. Clements,[7] J. S. Dunlop,[8] D. Farrah,[9] R. J. Ivison,[8,10] T. Jenness,[11,12] M. J. Michałowski,[8] E. I. Robson,[8,13] Douglas Scott,[14] J. Simpson,[8] M. Spaans[15] and P. van der Werf[16]

Affiliations are listed at the end of the paper

Accepted 2016 October 11. Received 2016 October 7; in original form 2016 June 2

ABSTRACT

We present deep observations at 450 and 850 μm in the Extended Groth Strip field taken with the SCUBA-2 camera mounted on the James Clerk Maxwell Telescope as part of the deep SCUBA-2 Cosmology Legacy Survey (S2CLS), achieving a central instrumental depth of $\sigma_{450} = 1.2$ mJy beam^{-1} and $\sigma_{850} = 0.2$ mJy beam^{-1}. We detect 57 sources at 450 μm and 90 at 850 μm with signal-to-noise ratio >3.5 over ∼70 arcmin^2. From these detections, we derive the number counts at flux densities $S_{450} > 4.0$ mJy and $S_{850} > 0.9$ mJy, which represent the deepest number counts at these wavelengths derived using directly extracted sources from only blank-field observations with a single-dish telescope. Our measurements smoothly connect the gap between previous shallower blank-field single-dish observations and deep interferometric ALMA results. We estimate the contribution of our SCUBA-2 detected galaxies to the cosmic infrared background (CIB), as well as the contribution of 24 μm-selected galaxies through a stacking technique, which add a total of 0.26 ± 0.03 and 0.07 ± 0.01 MJy sr^{-1}, at 450 and 850 μm, respectively. These surface brightnesses correspond to 60 ± 20 and 50 ± 20 per cent of the total CIB measurements, where the errors are dominated by those of the total CIB. Using the photometric redshifts of the 24 μm-selected sample and the redshift distributions of the submillimetre galaxies, we find that the redshift distribution of the recovered CIB is different at each wavelength, with a peak at $z \sim 1$ for 450 μm and at $z \sim 2$ for 850 μm, consistent with previous observations and theoretical models.

Key words: galaxies: evolution – galaxies: high-redshift – cosmology: observations – submillimetre: galaxies.

1 INTRODUCTION

Early studies of the cosmic infrared background (CIB) showed that the Universe emits a comparable energy density at infrared (IR) and submillimetre wavelengths as it does at optical and ultraviolet wavebands, which suggests that roughly half of the star light emission is absorbed and re-emitted by dust in galaxies (e.g. Soifer, Neugebauer & Houck 1987; Puget et al. 1996; Fixsen et al. 1998). The first attempt to resolve this background resulted in the discovery of a new population of high-redshift ($z \sim 2$–3) galaxies (hereafter submillimetre galaxies, SMGs) through single-dish telescope observations at submillimetre wavelengths (e.g. Smail, Ivison & Blain 1997; Barger et al. 1998; Hughes et al. 1998).

The discovery of copious numbers of SMGs has proven to be a significant challenge for theoretical models of galaxy evolution. However, despite their large far-infrared (FIR) luminosities ($\gtrsim 10^{12}$ L$_\odot$) and their large space density (higher than local ULIRGs), these galaxies only represent a fraction of the measured CIB (see reviews by Blain et al. 2002; Casey, Narayanan & Cooray 2014). Previous blank-field surveys resolved 20–40 per cent of the CIB at 850 μm (e.g. Eales et al. 2000; Coppin et al. 2006). Meanwhile, in cluster fields 50–100 per cent of the CIB is resolved, thanks to the effect of gravitational lensing (e.g. Smail et al. 1997; Cowie, Barger & Kneib 2002; Knudsen, van der Werf & Kneib 2008; Chen et al. 2013), suggesting that a large fraction of this background originates

⋆ E-mail: zavala@inaoep.mx

from faint sources ($S_{850} < 3$ mJy) whose number counts are not yet well constrained. At shorter wavelengths, closer to the peak of the CIB ($\lambda \approx 200$ μm; Fixsen et al. 1998), observations with the *Herschel Space Observatory* have resolved ∼75 per cent of the CIB at 100 and 160 μm (Berta et al. 2011; Magnelli et al. 2013). Nevertheless, at 250, 350 and 500 μm only a small fraction (<25 per cent; Oliver et al. 2010, 2012) has been resolved in individual galaxies, due to its much higher confusion limit, although, using statistical methods such as stacking and P(D), a significant larger fraction (≈40–70 per cent) can be associated with discrete sources (e.g. Glenn et al. 2010; Béthermin et al. 2012a; Viero et al. 2013b), with recent study suggesting a resolved fraction greater than 90 per cent (Viero et al. 2015, see also Section 5.1).

Consequently, deeper observations with higher angular resolution are still required to directly resolve and to completely understand the nature of this emission, as well as to fully determine the number counts of SMGs at fainter flux densities. These are some of the key science drivers for the SCUBA-2 Cosmology Legacy Survey (S2CLS), which exploits the capabilities of the SCUBA-2 camera (Holland et al. 2013), efficiently achieving large and deep (confusion-limited) maps at both 450 and 850 μm, simultaneously. At the shorter wavelength, the angular resolution is $\theta_{\rm FWHM} \sim 8$ arcsec, a factor of about 5 better than *Herschel* at 500 μm ($\theta_{\rm FWHM} \sim 36.6$ arcsec), which results in a confusion limit around seven times deeper.

On the other hand, the interferometric technique combined with the high sensitivity of the Atacama Large Millimeter/submillimeter Array (ALMA) has allowed the exploration of a range of flux densities unreachable through single-dish telescopes (e.g. Hatsukade et al. 2013; Ono et al. 2014; Carniani et al. 2015; Oteo et al. 2016; Aravena et al. 2016; Dunlop et al. 2016; Fujimoto et al. 2016). However, because of its relatively small field of view, it is observationally expensive to map large areas of blank sky with ALMA, and therefore difficult to constrain the less abundant population of bright galaxies. For these reasons, deep single-dish telescope observations are still necessary to bridge the gap between new deep interferometric results and the past single-dish shallower studies.

Here, we present 450 and 850 μm observations taken in the Extended Groth Strip (EGS) field as part of the deep tier of the S2CLS (the wide tier of the survey has been presented by Geach et al. 2016). This field has been the target of the All-wavelength Extended Groth strip International Survey (AEGIS), which includes observations of some of the world's most powerful telescopes, from X-rays to radio wavelengths. James Clerk Maxwell Telescope (JCMT) observations were scheduled to take advantage of excellent conditions ($\tau_{225\,\rm GHz} < 0.05$) at the top of Manua Kea, which results in the deepest single-dish telescope blank-field observations achieved at these wavelengths, comparable to the deep S2CLS maps in COSMOS and UDS (Geach et al. 2013; Roseboom et al. 2013; Koprowski et al. 2016).

In this paper, we report the first results of the EGS deep study. We describe the observations and data reduction in Section 2. The maps and source extraction are described in Section 3. In Section 4, we report the estimated number counts at each wavelength, and in Section 5 the CIB fraction recovered. Finally, our results are summarized in Section 6. The multiwavelength analysis, as well as a description of the physical properties of these galaxies will be presented in a subsequent paper (Zavala et al., in preparation).

All calculations assume a standard Λ cold dark matter cosmology with $\Omega_\Lambda = 0.68$, $\Omega_{\rm m} = 0.32$, and $H_0 = 67$ km s^{-1} Mpc^{-1} (Planck Collaboration XVI 2014).

2 OBSERVATIONS AND DATA REDUCTION

Observations at 450 and 850 μm were taken, simultaneously, with the SCUBA-2 camera on the JCMT between 2012 and 2015 under the best weather conditions (band 1, $\tau_{225\,\rm GHz} < 0.05$) as part of the deep S2CLS in the extragalactic EGS field. A standard ∼5 arcmin diameter 'DAISY' mapping pattern (Bintley et al. 2014) was used, which keeps the pointing centre on one of the four SCUBA-2 subarrays during the scanning. All data were reduced using the standard SMURF package (Jenness et al. 2011; Chapin et al. 2013) with the default 'blank-field' configuration, although the procedure for map-making (standardized across the S2CLS project) differs slightly from that described in section 4.2 of Chapin et al. (2013). This process is described in detail in Geach et al. (2013, 2016) which we summarize here, emphasizing the differences with Chapin et al. (2013).

The signal recorded by each bolometer is assumed to be a linear combination of atmospheric emission, astronomical signal (attenuated by atmospheric extinction), and a noise term. While extinction may be corrected directly using external measurements (i.e. extrapolating from $\tau_{225\,\rm GHz}$ measured at the adjacent Caltech Submillimeter Observatory), the dynamic iterative map maker attempts to solve for the remaining components, refining the model until convergence is met, at which either an acceptable tolerance has been reached, or a fixed number of iterations has been completed. First, all of the bolometer data are re-sampled to a lower data rate corresponding to the Nyquist frequency for the chosen pixel size, and filtered to retain only frequencies relevant to point-sources scales, which results in a band-pass filter defined as $v/150\,\text{arcsec} < f < v/4\,\text{arcsec}$, where f is in Hz, and v is the scan speed in arcsec s^{-1}. Then, each iteration consists of the following essential steps: (i) removing interbolometer correlated noise (primarily sky emission) via common-mode suppression (subtracting a time-varying template created from the average of all bolometer signals in a given subarray, using per-bolometer gains and offsets to fit it to the signal in question prior to removal); (ii) producing maps (on 2 arcsec × 2 arcsec pixel grids) from the resulting time streams which should, ideally, consist only of astronomical sources and higher frequency (un-correlated) noise; and finally (iii) re-projecting the map back into the time-domain to estimate the contribution of astronomical sources to the bolometer signals (e.g. 'scanning' the detectors across the current map estimate), and then subtracting these signals, leaving primarily high frequency, uncorrelated noise from which a time-domain variance can be measured for each bolometer. The variance measured in step (iii) is used to weight the data in step (ii) in subsequent iterations. We also note that the common-mode subtraction step in (i) provides an efficient mechanism for flagging bad data: portions of bolometer signals that do not resemble the common-mode are simply masked and ignored in the remaining analysis. Since the signal-to-noise ratio (S/N) of astronomical sources is low in these fields (generally undetectable in a single bolometer signal), the solutions converge quickly. The map-maker halts when the reduced χ^2 changes by less than 0.05, or a maximum of 20 iterations has been reached. We note that the maps are quite insensitive to the values of these convergence criteria provided that a handful of iterations are completed.

The maps produced by this procedure continue to exhibit weak large-scale noise features (though on scales smaller than the 150 arcsec cutoff in the initial band-pass filter) due to any non-white noise that may have gotten through the common-mode subtraction step. Chapin et al. (2013) advocates using jackknife maps at this stage to empirically measure this noise (i.e. dividing the data into two halves, producing maps of each, and then taking their difference to

yield a map containing only noise without astronomical sources), and then constructing a 'whitening filter' to flatten the map to assist with source detection. While in some sense optimal, this procedure will produce a different effective point spread function (PSF) for each observation, making comparison between this field and others in the S2CLS more complicated. For this reason, across the S2CLS, we have opted to use a slightly more conservative (and uniform) method of large-scale noise suppression which involves subtracting a low-pass filtered map (accomplished by smoothing the map with a 30 arcsec full width at half-maximum – FWHM – Gaussian kernel). This method has been used by virtually all groups analysing fields of point sources observed with SCUBA-2 data to date. In other areas of astronomy, this procedure is known as a linear unsharp mask.

Finally, in order to detect sources, we apply a matched filter to the maps, using an effective PSF constructed from an estimate of the diffraction-limited SCUBA-2 beams (Gaussians, with $\theta_{\rm FWHM} \approx 8$ and 14.5 arcsec for the 450 and 850 μm bands, respectively; Dempsey et al. 2013), filtered using the same 30 arcsec FWHM background subtraction kernel (which introduces negative side-lobes). Note that this procedure is only optimal in the case that point sources are isolated in fields of uncorrelated white noise. A more sophisticated 'confusion-compensating' matched filter was proposed in Chapin et al. (2011) in which the effects of source blending are included explicitly in the estimate of the noise power spectrum, which in turn leads to a point-source detection kernel that behaves as the PSF described here in the low-S/N regime (when considering only instrumental noise), and smoothly converges to a de-convolution operator in the limit of infinite S/N. However, since this more optimal filter is a function of both the S/N of the observations and an estimate of the source counts in the field, it would again lead to complications when comparing different S2CLS fields. For this reason, we have opted for this simpler, uniform source-finding kernel across the project.

2.1 Astrometry

The identification of radio counterparts has been used to improve the astrometric accuracy of the submillimetre maps and to measure positional uncertainty of SMGs (e.g. Ivison et al. 2002; Chapman et al. 2005). We use the VLA/EGS 20-cm survey (Ivison et al. 2007b) for this purpose. The position of the sources in this catalogue are adopted to stack the signal in our beam-convolved SCUBA-2 maps. Fig. 1 shows 30 arcsec × 30 arcsec postage stamps extracted from regions centred at the radio positions and stacked together. The stacked signal peaks at the central pixel in the co-added postage stamps, indicating that there is no systematic offset between the SCUBA-2 data and the radio catalogue, or if it exists, is less than our pixel size (2 arcsec × 2 arcsec). Therefore, no positional correction was applied.

Since the stacking could be dominated by a few bright sources, we repeated the procedure but re-normalizing each image to a constant peak brightness, finding consistent results.

3 MAPS AND SOURCE CATALOGUE

3.1 Maps

The 450 and 850 μm S/N maps of EGS acquired with SCUBA-2 on the JCMT are shown in Fig. 2. Each map has a radially varying coverage (see contours in Fig. 2), which is roughly uniform over the central ∼2 arcmin and increases radially towards the edge of the map as the effective exposure time decreases. The maximum

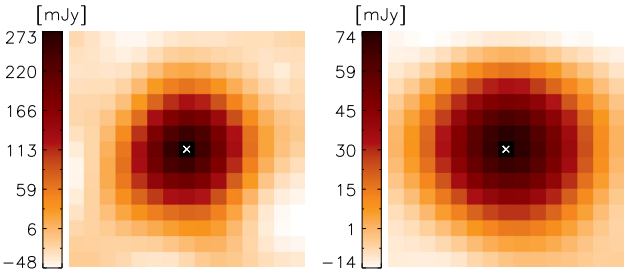

Figure 1. 30 arcsec × 30 arcsec co-added postage stamps of the SCUBA-2 450 and 850 μm flux maps (left and right, respectively) extracted from regions centred at 39 radio source positions that lie within the SCUBA-2 map boundary (Ivison et al. 2007b). The stacked signal peaks at the central pixel for each map (white cross) which means that the astrometry of the observations is better than the 2 arcsec pixel-size. The FHWM of the best-fitting Gaussian at 450 μm is 11 arcsec × 12 arcsec, and 14.5 arcsec × 16 arcsec at 850 μm. The ∼30 per cent broadening over the nominal 450 μm FWHM of the PSF can be explained by a multiplicity of 20–30 per cent (as previously reported by interferometric results; e.g. Ivison et al. 2007a; Wang et al. 2011; Hodge et al. 2013) where the secondary source only contributes ∼20 per cent of the total flux density.

instrumental depth achieved in the centre of each map is 1.2 and 0.2 mJy beam^{-1} at 450 and 850 μm, respectively. The noise has been estimated through a jackknife procedure where 50 per cent of the individual scans are inverted. The total area considered for source extraction is ≈70 arcmin^2, where the rms noise is below 2.5 and 0.5 mJy beam^{-1}, respectively.

3.2 Source extraction and source catalogue

To identify source candidates, we search for pixels in the (beam convolved) S/N map with values >3.0. If a peak is found, we adopt the celestial coordinates of the pixel, the flux density and the noise, and subtract the PSF estimated in the map-making procedure scaled to the S/N measured at this position. The process is repeated until there are no more pixels with S/N > 3.0. All the source candidates above this threshold are listed in Table A2, together with their coordinates, measured S/N, raw flux densities, and deboosted flux densities (see Section 3.4). However, a conservative threshold of S/N > 3.5 has been adopted to define a more robust sample. The 3.5 threshold value is chosen to be the S/N level at which the contamination rate due to false detection is estimated to be less than 5 per cent at 850 μm and less than 10 per cent at 450 μm. At this threshold, we detect 57 sources at 450 μm and 90 at 850 μm. These sources are marked with squares in Fig. 2.

3.3 Completeness and positional uncertainty

The detection rate for a given source within a flux density range is affected by both confusion noise from the underlying population of faint sources and instrumental Gaussian noise in the map. To account for these effects, we estimate the completeness of source detection using simulations in which mock sources with different flux densities are inserted into the observed EGS/SCUBA-2 signal maps, and then recovered with the same source extraction procedure used for the real catalogue. As described in detail by Scott et al. (2008, 2010), this method has the benefit of taking into account the effects of random and confusion noise in the signal map and, since the sources are inserted one at a time, it does not modify the properties of the real map. We insert 10 000 sources in each flux density bin, ranging from 1 to 20 mJy (in bins of 0.5 mJy) for the

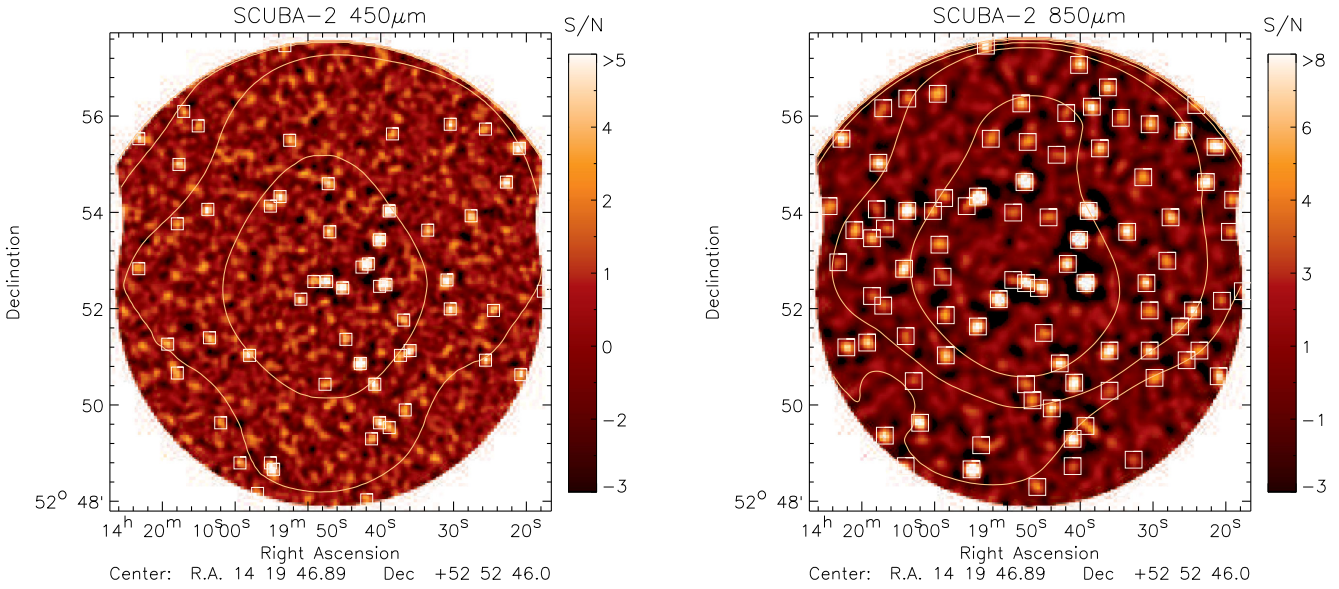

Figure 2. The 450 and 850 μm Extended Groth Strip SCUBA-2 S/N maps over an area of ≈70 arcmin^2. The yellow contours show the variation in the noise level, and are spaced at 0.4 and 0.05 mJy for the 450 and 850 μm maps and starting at 1.5 and 0.25 mJy, respectively. The identified S/N > 3.5 sources candidates are marked with yellow squares in both maps. The maps have been scaled to emphasize the visibility of the detected sources.

450 μm map and from 0.1 to 5 mJy (in bins of 0.1 mJy) for the 850 μm map. A source is considered recovered if it is extracted with S/N > 3.5 at a radius <1.5 times the size of the corresponding beam of its input position. Fig. 3 shows the completeness fraction as a function of flux density for this survey.

On the other hand, the relatively large beam-size combined with the low S/N of the detections results in a significant error on the position of the source candidates. We characterize the positional uncertainty as a function of S/N from the same simulations, where now we focus on the distance at which the artificial sources were extracted. The positions of the simulated sources are chosen randomly within a pixel (instead of adopting the pixel centre) in order to take into account the 2 arcsec × 2 arcsec pixel size. Fig. 3 also shows the median positional offset between the measured output source position and its input position as a function of S/N.

3.4 Flux deboosting

When sources are detected at low S/N, their measured flux densities are systematically larger than their intrinsic flux densities if the number of sources increases while decreasing flux (e.g. Hogg & Turner 1998). In this case, it becomes more likely that the numerous faint sources are boosted higher than the rarer bright sources to lower fluxes. This is particularly important in surveys of SMGs since the intrinsic population is known to have a steep distribution of counts, and also because the galaxies are typically detected at low S/N.

In addition to the completeness and positional uncertainties, the simulations described above allow us to calculate the boosting factor. This 'flux boosting' is measured as the ratio of the output measured flux density and the input flux density, as shown in Fig. 3. The boosting factor can also be estimated as a function of both S/N and the local noise in the map, selecting only the simulated sources that have been inserted in specific regions within a specific noise range. This selection is important, as we know that our maps have radially varying sensitivity. The error in the deboosting factor is estimated as the standard deviation in each bin of S/N and noise, and then is propagated to estimate the error in the deboosted flux density.

An alternative statistical method has been developed to correct the flux boosting. For each source candidate, we can estimate a posterior flux distribution (PFD) which describes the intrinsic flux density of the source in terms of probabilities. The PFD is calculated using the Bayesian approach of Coppin et al. (2005, 2006). For an individual source detected with measured flux density $S_m \pm \sigma_m$, the probability distribution for its intrinsic flux density S_i is given by

$$p(S_i|S_m, \sigma_m) = \frac{p(S_i)p(S_m, \sigma_m|S_i)}{p(S_m, \sigma_m)}, \quad (1)$$

where $p(S_i)$ is the prior distribution of flux densities, $p(S_m, \sigma_m|S_i)$ is the likelihood of observing the data and $p(S_m, \sigma_m)$ is a normalization factor. We assume a Gaussian noise distribution for the likelihood of observing the data, where

$$p(S_m, \sigma_m|S_i) = \frac{1}{\sqrt{2\pi\sigma_m^2}} \exp\left[\frac{-(S_m - S_i)^2}{2\sigma_m^2}\right]. \quad (2)$$

This assumption is justified by the Gaussian flux distribution observed in jackknife noise maps of our EGS data (see also Geach et al. 2013).

The prior distribution of flux densities $p(S_i)$ is estimated by generating 10 000 noiseless sky realizations, where sources are inserted with a uniform spatial distribution into a blank map according to a number counts distribution. Each source is assumed to be the PSF scaled by the flux density. The pixel histogram of flux values from all these realizations gives an estimate of $p(S_i)$. We assume the prior number counts to be a Schechter function with the best-fitting parameters for the SCUBA-2 450 and 850 μm COSMOS number counts from Casey et al. (2013) or Geach et al. (2013). We find no significant differences between the PFDs of sources estimated when using these different priors.

The deboosted flux density for each source is assumed to be the maximum value of the PFD and its associated 68 per cent confidence interval. We have compared the deboosted flux density for each source estimated using both methods, i.e. Monte Carlo simulations and the Bayesian PFD. As we can see in Fig. 4, the results of both methods are in good agreement.

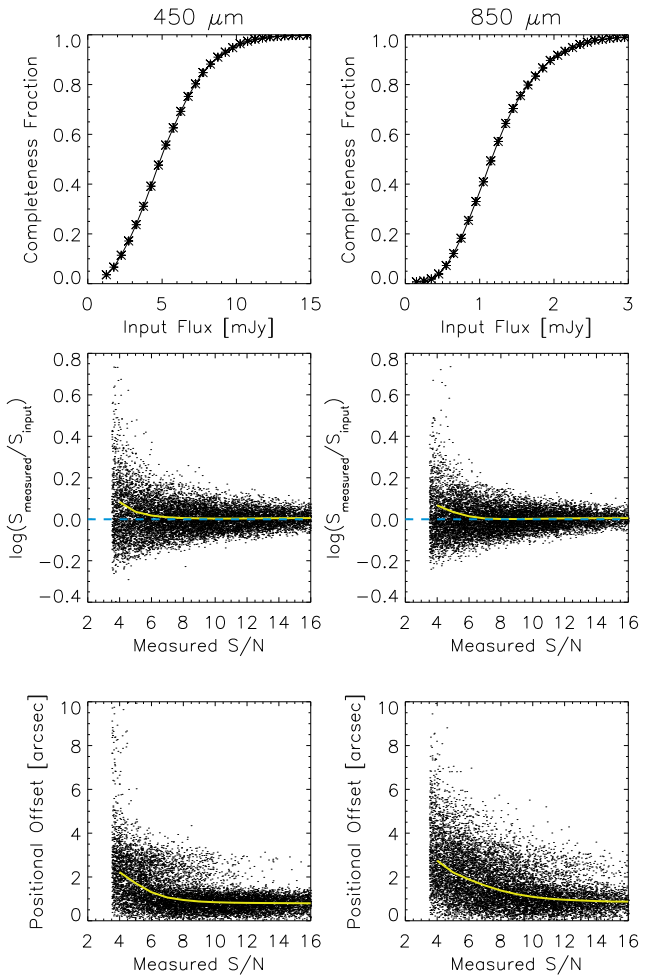

Figure 3. Top: completeness of the 450 (left) and 850 μm (right) source catalogues as a function of flux density. The points and error bars show the completeness estimated by inserting sources of known flux density one at a time into the observed signal maps and then finding them with the same source extraction algorithm used to create the source catalogue. Middle: the boosting factor estimated from the same set of simulations, measured as the ratio of output measured flux density and input flux density. The yellow solid line represents the median boosting factor in each bin of S/N and the blue dashed line represents no flux boosting. Bottom: positional uncertainty as a function of S/N, calculated as the offset between the measured output position and its input position. The yellow line represents the median value in each bin of S/N.

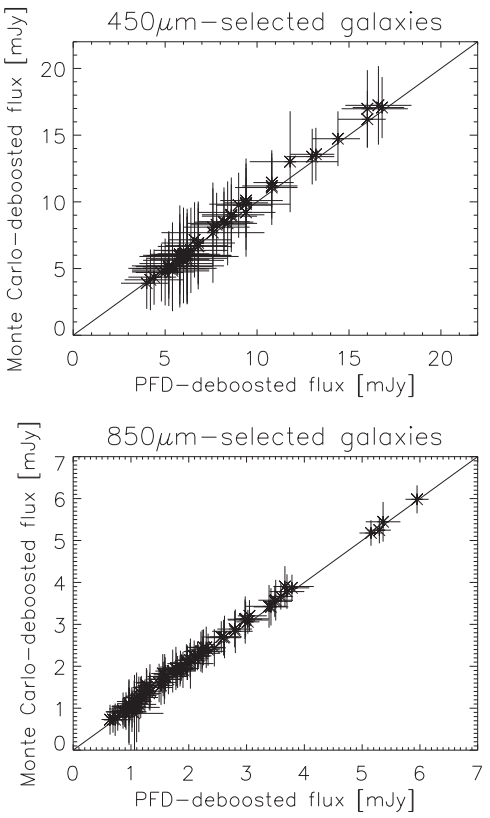

Figure 4. Comparison between the deboosted flux density of the source candidates detected at S/N > 3.5 (top: 450 μm, bottom: 850 μm), estimated through Monte Carlo simulations and the Bayesian method.

Finally, from the PFD, we measure the probability that each source candidate will be deboosted to less than 0 mJy. This value could be used to exclude candidates that exceed some probability threshold, and therefore decrease the contamination of false sources in our catalogue (see Section 4).

4 NUMBER COUNTS

The cumulative number counts (also called 'source counts') describe the number density of galaxies as a function of flux density. To derive this quantity, we adopt the standard bootstrap sampling method that has been extensively used by different authors (e.g. Coppin et al. 2005, 2006; Austermann et al. 2009, 2010). While other techniques commonly used for the extraction of number counts can in principle estimate the counts at fainter flux densities (for example the '*P(D)*' technique; Patanchon et al. 2009; Glenn et al. 2010), it has been claimed that they are more dependent on the assumed model (see discussion in Scott et al. 2010), require constant instrumental noise across the image (which is not our case) and a good understanding of the instrumental PSF and source clustering (e.g. Vernstrom et al. 2014). On the other hand, with the Bayesian approach, the estimated counts are only weakly dependent on the assumed model of the prior distribution (Austermann et al. 2009, 2010). Since this method is described in detail in the aforementioned papers, we only briefly summarize it here.

Using the source catalogue constructed from all the source candidates with S/N > 3.0 and following the procedure described in Section 3.4, we derive the PFD for each source candidate. In each realization, we randomly assign flux densities to the sources in the catalogue according to their respective PFD, and then the sources are binned to derive the differential (dN/dS) and cumulative [$N(>S)$] number counts, correcting each bin by the corresponding completeness and dividing by the survey area. To avoid including a large number of false positives, we only include sources whose PFD indicates a probability of less than 5 per cent of having a negative intrinsic flux, $P(S < 0) \leq 0.05$. This process is repeated 500 times, also taking into account the error in completeness, in order to sufficiently sample the number count probability distribution.

We calculate the number counts at 450 μm for flux densities ≥4 mJy and at 850 μm for flux densities ≥0.9 mJy. At lower flux densities, the level of completeness is too low (≤25 per cent), and therefore, the errors could be large. These represent the deepest number counts derived from single-dish telescope observations towards a blank field (i.e. without the benefit of lens amplification).

Table 1. Differential and cumulative number counts at 450 and 850 μm, calculated as described in Section 4, along with the best-fitting parameters.

450 μm-number counts				*850 μm-number counts*			
S (mJy)	dN/dS^a ($mJy^{-1}deg^{-2}$)	S (mJy)	$N(>S)$ (deg^{-2})	S (mJy)	dN/dS^a ($mJy^{-1}deg^{-2}$)	S (mJy)	$N(>S)$ (deg^{-2})
6.0	873 ± 100	4.0	4742 ± 360	1.4	4076 ± 400	0.9	6106 ± 450
10	207 ± 45	8.0	1250 ± 186	2.4	1210 ± 180	1.9	2030 ± 140
14	76 ± 20	12	423 ± 104	3.4	559 ± 100	2.9	820 ± 90
18	29 ± 16	16	119 ± 40	4.9	117 ± 20	3.9	261 ± 33
Best-fitting Schechter function using all data							
N_0	S_0	α		N_0	S_0	α	
7100 ± 600	8.9 ± 1.5	2.6 ± 0.2		8300 ± 300	2.3 ± 0.5	2.6 ± 0.8	
Best-fitting double-power law using all data							
N_0	S_0	α	β	N_0	S_0	α	β
600 ± 140	23 ± 4	2.5 ± 0.2	6.5 ± 0.2	1900 ± 600	4.3 ± 0.5	2.0 ± 0.4	6.0 ± 0.3
Best-fitting Schechter function using only S2CLS data							
N_0	S_0	α		N_0	S_0	α	
4400 ± 2300	11 ± 4	3.1 ± 0.3		$16\,000 \pm 4000$	1.3 ± 0.5	1.7 ± 0.8	

[a]The differential number counts reported in the table are not Euclidean-normalized.

It is important to remark that the confusion noise in this map has been measured to be $\sigma_c \approx 0.4$ mJy beam^{-1} at 850 μm, which is comparable to the instrumental noise in the map, and therefore should be taken into account. Following the results of Scott et al. (2010), we have estimated the completeness by inserting mock sources one at a time in the real flux maps (see Section 3.3). This method has the advantage of taking into account the confusion effects, since the sources are inserted in the real map, and does not overpredict the completeness, as when the sources are inserted into noise maps, as is commonly done in the literature.

Table 1 lists the resulting bin centres, differential and cumulative number counts, and 68 per cent confidence interval uncertainties. Fig. 5 shows the cumulative and differential number counts at each wavelength.

We describe the differential number counts by a Schechter-like function of the form

$$\frac{dN}{dS} = \left(\frac{N_0}{S_0}\right)\left(\frac{S}{S_0}\right)^{1-\alpha} \exp\left(-\frac{S}{S_0}\right). \quad (3)$$

Alternatively, the number counts can also be fit with a double-power law described by

$$\frac{dN}{dS} = \frac{N_0}{S_0}\left[\left(\frac{S}{S_0}\right)^{\alpha} + \left(\frac{S}{S_0}\right)^{\beta}\right]^{-1}, \quad (4)$$

where N_0, S_0, α and β describe the normalization, break, and slope of the power laws, respectively.

To determine the best-fitting parameters, we perform a χ^2 optimization using a Levenberg–Marquardt algorithm. In order to better determine the best-fitting parameters, we include the results from other surveys in the fitting. At 450 μm, we use all the SCUBA-2 measurements (Casey et al. 2013; Chen et al. 2013; Geach et al. 2013), which cover a flux density range of $S_{450} \approx$ 1–40 mJy. We exclude results from *Herschel* surveys at higher flux densities, since these estimates are dominated by the lensed population. At 850 μm, we complement our measurements at fainter flux densities with the results from SCUBA-2 observations in lensed fields (Chen et al. 2013). However, we exclude the estimates of Fujimoto et al. (2016) because of the additional uncertainty in the 1.2 mm-to-850 μm scale factor. At higher flux densities, we complement our measurements with the results of ALMA observations (Karim et al. 2013; Simpson et al. 2015), and exclude the rest of the single-dish measurements, since effects of blending are more significant at these high flux densities.

The best-fitting parameters for both models are listed in Table 1 and plotted in Fig. 5. The errors were estimated through Monte Carlo simulations. We find that both functional forms (Schechter-like and double-power law) produce similar fits.

The last bin of our 450 μm cumulative number counts lies below our best-fitting function. This is because we did not find any source with $S_{450} > 18$ mJy, most likely due to cosmic variance in our relatively small map.

4.1 Comparison to other surveys

We compare our number counts at both wavelengths to the results of previously published surveys in Fig. 5.

At 450 μm, our results are in very good agreement with the counts from the previous S2CLS map in the COSMOS field (Geach et al. 2013), which has similar depth and area. In the same field, Casey et al. (2013) presented wider but shallower observations, which allowed them to estimate the number counts to brighter flux densities, and are also consistent with our values. Chen et al. (2013) and Hsu et al. (2016) combined data from cluster lensed fields and blank fields, measuring the counts over a wide flux density range. Our estimates are consistent with their results, as well as with our extrapolation of the Schechter function. At flux densities above ∼20 mJy, the number counts from our observations could be compared with the results from *Herschel* surveys, which mapped wider areas at 500 μm to shallower depths. Our results are in agreement with the values reported by Oliver et al. (2010) and Clements et al. (2010) at ∼20 mJy, where the distributions meet. At higher flux densities, the counts estimated using *Herschel* are dominated by rare bright and lensed galaxies that our smaller area map cannot constrain.

At 850 μm, the measurements from our survey are in agreement with the values of Chen et al. (2013) and Hsu et al. (2016), which came from both lensed and blank fields, except for the brighter flux density bins ($\gtrsim$7 mJy), in which our extrapolation of the Schechter function lies below their estimates. The same is

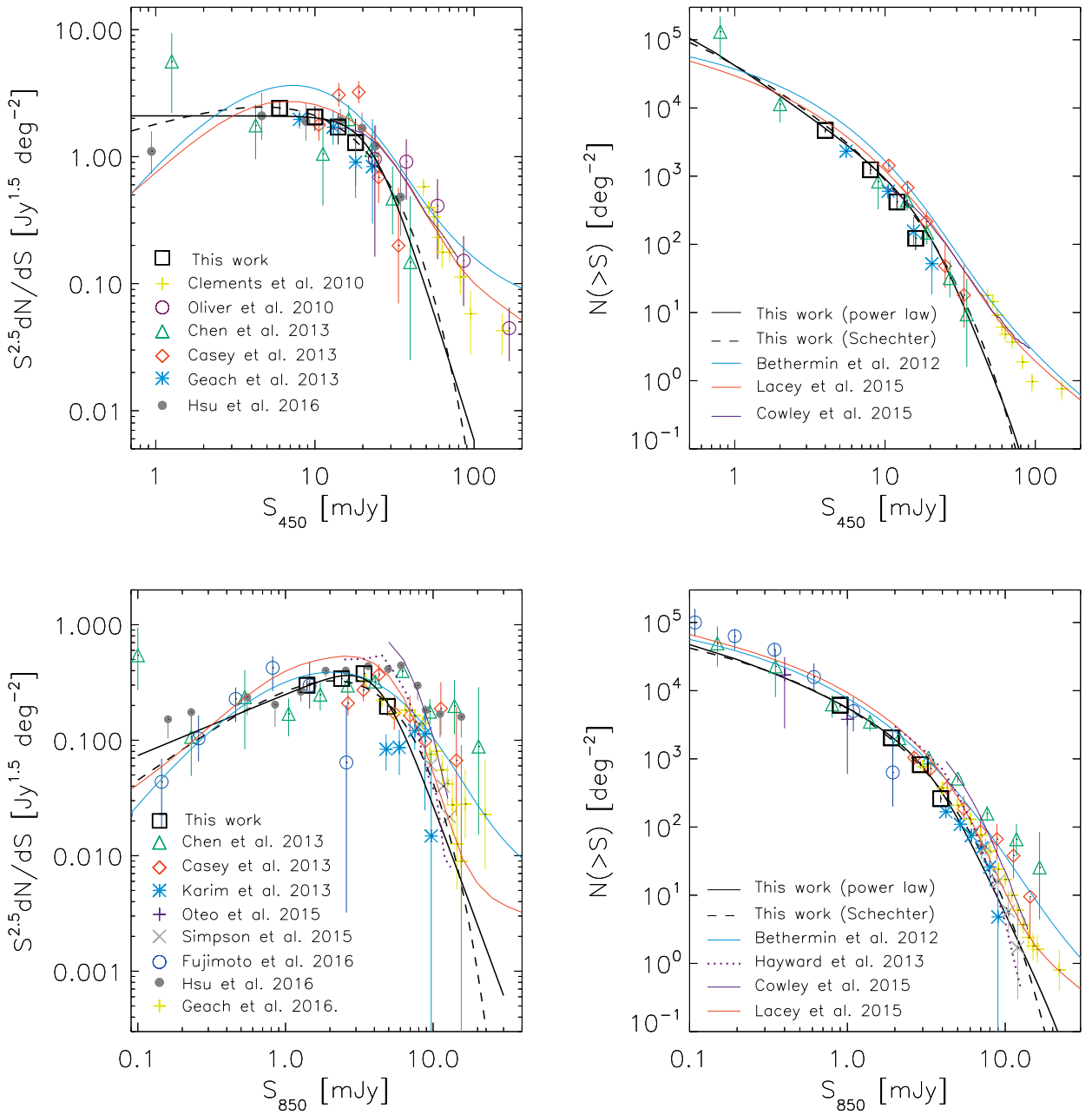

Figure 5. Left: Euclidean-normalized differential number counts of galaxies detected at 450 (top) and 850 μm (bottom). Error bars indicate the 68 per cent confidence intervals. The solid black line represents the best fit using a double-power law, and the dashed black line is the best fit using a Schechter-like function to the data described in Section 4. For comparison, we also plot the results from other studies and some theoretical predictions from the literature. Right: corresponding cumulative number counts at 450 (top) and 850 μm (bottom) together with integrated fits.

true for the Casey et al. (2013) results. On the other hand, at such high flux densities our extrapolation of the Schechter function is in good agreement with recent results from follow-up ALMA observations of SMGs detected with single-dish telescopes (Karim et al. 2013; Simpson et al. 2015), and with the number counts derived from ∼5 deg^2 SCUBA-2 observations (the largest and deepest single survey at 850 μm so far; Geach et al. 2016). At fainter flux densities, our results overlap with the deep 870 μm ALMA observations presented by Oteo et al. (2016) in excellent agreement, although their uncertainties are large because of the small number of sources detected (11 sources in ∼6 $arcmin^2$ combining ALMA observations at different depths). At the same time, our estimations are consistent with the results at 1.2 mm (scaled to 850 μm by a factor of 2.3, assuming a typical spectral energy distribution – SED – at $z \sim 2$) by Fujimoto et al. (2016), which include all the archival deep data at that time (including data from other deep ALMA observations, e.g. Hatsukade et al. 2013; Ono et al. 2014; Carniani et al. 2015), compiling a sample of 133 sources within ∼10 $arcmin^2$.

Excluding the results from Chen et al. (2013) and Hsu et al. (2016), which use the benefit of lensing amplification, this is the first time that single-dish blank-field observations have connected with

the results from deep interferometric measurements. This results in a better understanding of the number counts towards fainter flux densities.

Since we have included previously reported number counts in our fits, it may not be surprising that our results are in agreement with previous estimates of the number counts. To test if our data alone are in good agreement with previous results, we again run the fitting procedure, but just using our measurements. Here, we only apply the Schechter function since the double-power law has one more free parameter, making it impractical to fit to just four bins. The best-fitting parameters are listed in Table 1. At 450 μm, although the parameters of the Schechter function are different, the fit is in very good agreement with the values in the literature, from about 1 to 40 mJy. At 850 μm, our measurements are in good agreement with the brighter flux density estimations, however, at fainter flux densities (<0.5 mJy) our extrapolation of the Schechter function is below the measurements of Chen et al. (2013, although still consistent within the error bars), but in very good agreement with the ALMA estimates of Oteo et al. (2016).

4.2 Comparison to models

In this section, we compare the 450 and 850 μm number counts presented in this work to the results of recent galaxy formation models. Lacey et al. (2016) presented a new version of the GALFORM semi-analytical model, which includes improvements to the prescription for AGN feedback, disc-instability-driven starbursts, and stellar population models. Cowley et al. (2015) implemented also the effect of the beam-size on the observed number counts on the GALFORM model to study the possible bias introduced by the source blending of individual sources. However, they conclude that the beam size at 450 μm does not produce any significant enhancement of the source density. In Fig. 5, it can be seen that the number counts predicted by GALFORM appear to be in broad agreement with the results presented here within the 450 μm flux density range of $S_{450} = 3$–30 mJy. However, while the shape of the number counts are broadly similar we identify a small offset between the observed counts and the theoretical predictions, where the GALFORM source density lie a factor of ∼1.3 above our integrated measurements. In contrast, at the faintest flux, the model underpredicts the number of sources (a factor ∼2 in the cumulative number counts at $S_{450} \approx 0.6$ mJy). At higher flux densities, the number counts become dominated by the lensed population that, as described in the previous section, our survey has insufficient area coverage to constrain accurately. We also compare to the Béthermin et al. (2012b) model, which is based on the evolution of the main sequence of star-forming galaxies and a second population of starburst galaxies, assuming some SED templates. The results of Béthermin et al. (2012b) are similar to the GALFORM model and therefore are in reasonable agreement with our measurements, albeit with a marginally larger offset of ∼1.7 above our cumulative counts (Fig. 5.)

At 850 μm, the number counts predicted by the GALFORM model (Lacey et al. 2016) also follow the behaviour of our best-fitting source counts at flux density of $S_{850} = 0.2$–10 mJy. Although, we again note that the theoretical counts are systematically a factor ∼1.5 above the observed values. Interferometric observations have shown that the source blending at this wavelength is more important due to the larger beam-size (e.g. Wang et al. 2011; Hodge et al. 2013). This effect is also predicted by Cowley et al. (2015) when taking into account the coarser angular resolution in the GALFORM model. The Béthermin et al. (2012b) predictions are also in agreement (but also a factor ∼1.4 above our best-fitting integrated functions), nevertheless, when compared with our estimates and the Geach et al. (2016) results, the model overpredicts the counts at $S_{850} \gtrsim 8$ mJy, for example, by a factor of ∼5 in the cumulative counts at $S_{850} \approx 16$ mJy (see Fig. 5). Finally, we also compare our measurements to the model of Hayward et al. (2013) based on the *bolshoi* cosmological simulation, which also takes into account the blending in single-dish observations. The predictions for a 15 arcsec beam are consistent with our number counts, however, this model predicts that the multiplicity caused by blending increases the number counts by more than an order of magnitude. This has been ruled out by recent interferometric results which found that the number counts are boosted by only 20 per cent at $S_{870} > 7.5$ mJy, and 60 per cent at $S_{870} > 12$ mJy (Simpson et al. 2015).

5 CONTRIBUTION TO THE CIB

5.1 The resolved CIB

Once we have extracted the point sources with S/N > 3.5 from our maps, we can estimate the contribution of these sources to the CIB at each wavelength, corrected for completeness, by integrating the number counts above our flux density limit. To do this, we integrate the best-fitting number counts (those derived when used all the data) at $S_{450} > 4.0$ mJy and $S_{850} > 0.9$ mJy. At these flux densities, the integration of both the double-power law and the Schechter function give us the same results. The integrated intensities of our detected galaxies are $I_\nu(450\,\mu\text{m}) = (0.13 \pm 0.03$ MJy sr^{-1} and $I_\nu(850\,\mu\text{m}) = 0.04 \pm 0.01$ MJy sr^{-1}, which correspond to 28 ± 13 and 28 ± 14 per cent, respectively, of the CIB measured by the *COBE* Far-Infrared Absolute Spectrophotometer (FIRAS; Fixsen et al. 1998), where the uncertainties are dominated by those of the total CIB values. Extrapolating the number counts below our detection limits, we find that the total CIB is resolved at $S_{450} \approx 0.6$ mJy and $S_{850} \approx 0.02$ mJy, respectively.

There have been other measurements of the total values of the CIB based on both direct measurements, for example, of *COBE* Diffuse Infrared Background Experiment (DIRBE; Hauser et al. 1998) and *COBE* FIRAS (Lagache et al. 1999), and integrated galaxy-counts derived from *Spitzer* and *Herschel* (e.g. Dole et al. 2006; Berta et al. 2011; Béthermin et al. 2012a; see also recent compilation by Driver et al. 2016). However, the uncertainties remain large, and therefore, better estimates of the absolutes CIB values are still required to better constrain the fraction contributed by these galaxies. Here, we adopt the values of Fixsen et al. (1998) in order to consistently compare our results to previous similar studies (e.g. Viero et al. 2015).

To measure the contribution to the CIB by galaxies fainter than our detection threshold, we stack the maps at the positions of 24 μm galaxies selected from a *Spitzer* catalogue in the EGS field (Barro et al. 2011a,b). This technique has been implemented before by different authors (e.g. Marsden et al. 2009; Béthermin et al. 2012a; Viero et al. 2013b; and references therein), and used by Geach et al. (2013) in the COSMOS/S2CLS survey. First, we remove point sources detected with S/N > 3.5 from the maps using a PSF normalized to the flux of each individual source in our catalogue. Then, we subtract the mean of the SCUBA-2 maps, which yields a residual map, where the flux corresponds to sources that are not present in our catalogues (in addition to noise). Finally, the 450 and 850 μm maps are stacked at the position of the 24 μm sources, averaging the flux at each position.

Since the 24 μm source catalogue includes photometric redshifts, we can estimate the stacked flux density as a function of redshift,

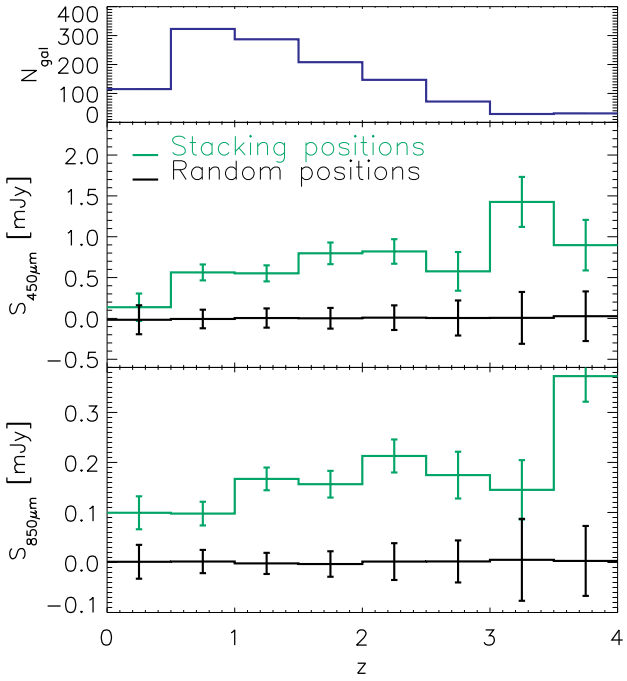

Figure 6. Stacked average flux density at 450 and 850 μm (green line in the middle and bottom panels, respectively) as a function of redshift at the position of the 24 μm-selected galaxy sample. The top panel represents the number of galaxies in bins of redshift used in the stacking procedure. The black lines represent the results of null tests, in which the stacking was done at random positions, finding an average stacked flux of zero.

as shown in Fig. 6. The uncertainty is estimated as $\sigma/\sqrt{N}$, with σ being the standard deviation in the stack and N the sample size (which is represented in the top panel of Fig. 6). To ensure that the recovered stacked flux comes from the 24 μm sample and not from noise or other contaminants, we repeat the same procedure but at random positions, conserving the number of stacked positions in each redshift bin. As shown in Fig. 6, the average stacked flux from the random positions is zero, which means that the recovered fluxes are actually associated with the 24 μm population.

The total intensities recovered by the stacking are $I_\nu(450\,\mu\text{m}) = 0.13 \pm 0.01$ MJy sr^{-1} and $I_\nu(850\,\mu\text{m}) = 0.03 \pm 0.003$ MJy sr^{-1}, which corresponds to 28 ± 11 and 21 ± 9 per cent of the CIB, respectively, including the uncertainties in the absolute CIB values.

The contribution of the directly detected sources and the stacking of 24 μm galaxies amount to a total of0.26 ± 0.03 and 0.07 ± 0.01 MJy sr^{-1} at 450 and 850 μm, respectively, which correspond to ∼60 ± 20 and 50 ± 20 per cent of the total CIB measurements. This is in excellent agreement with the estimations by Béthermin et al. (2012a), who using the 24 μm sources as priors, estimating that the emission of galaxies down to ∼2 mJy at 500 μm contributed ∼55 per cent of the CIB.

An important concern in the stacking technique is the possible bias due to clustering, which can result in a boosted average flux density arising from faint, companion (or clustered) galaxies (e.g. Serjeant et al. 2008; Kurczynski & Gawiser 2010; Heinis et al. 2013). This effect increases with the size of the beam. However, using a 24 μm catalogue and the *Herschel* maps, Béthermin et al. (2012a) found that this bias is only 5–7 per cent at 250 μm, which has FWHM = 18.1 arcsec. Our 850 μm beam has FWHM = 14.5 arcsec, and therefore, the expected bias due to clustering should be less than 5 per cent (and even less at 450 μm with a beamsize of FWHM = 8 arcsec). Given the uncertainties in our measurements and the absolute values of the CIB, we have not included any clustering correction in our estimations.

Considering that roughly half of the CIB is still missing at both wavelengths, it is important to discuss the possible origin for this missing fraction. The first point to consider is that we do not correct our stacking measurements for the completeness of the 24 μm-selected catalogue. As discussed in earlier studies (e.g. Béthermin et al. 2012a), the stacking of an incomplete catalogue biases the result, missing a significant fraction of the intensity. Béthermin et al. (2013) show that an $S_{24\,\mu\text{m}} > 80$ μJy selection could miss up to half of the intensity expected from all galaxies, which could account for the remaining CIB.

Actually, Viero et al. (2015) studied the contribution of galaxies which are not detected in current near-IR surveys, for example, very low mass or very dusty galaxies, but which are correlated (i.e. clustered) with the detected galaxies. To account for these uncatalogued sources, they intentionally smoothed and stacked *Herschel* observations. They found that the contribution of these galaxies is very important, especially in the $1 < z < 4$ range (where the completeness is low), and could fully explain the rest of CIB at 250–500 μm. However, at longer wavelengths (i.e. $\lambda \gtrsim 850$ μm), deep interferometric observations (e.g. Chen et al. 2014; Fujimoto et al. 2016) have shown that only ∼50 per cent of the faint SMGs ($S_{850} \lesssim 2$ mJy) are detected in deep optical/NIR surveys, suggesting that many of these sources, which also contribute to the CIB, are high-redshift galaxies ($z \gtrsim 3$).

5.2 The redshift distribution of the recovered CIB

As described above, the stacking analysis was performed in bins of redshifts, which allowed us to estimate the contribution of these galaxies as a function of redshift. The green line in Fig. 7 represents the redshift distribution of the recovered intensity from the stacking of 24 μm prior positions at 450 and 850 μm.

To estimate the redshift distribution of the intensity produced by the galaxies formally detected in our SCUBA-2 maps, we adopt previously published redshift distributions of similar populations. For the 450 μm-detected galaxies, we use the distribution of Roseboom et al. (2013), which comprises photometric redshifts of 450 μm-selected galaxies detected in deep SCUBA-2 observations ($\sigma_{450} = 1.5$ mJy), similar to the depth of our map, and therefore, galaxies with similar flux densities. This redshift distribution shows a broad peak in the range $1 < z < 3$, and a median of $z = 1.4$ (Roseboom et al. 2013). For the 850 μm galaxies, we consider the redshift distribution of Chen et al. (2016), derived from a large sample of SCUBA-2-detected galaxies with $S_{850} > 1$ mJy, which has a median redshift of 2.6 ± 0.1, in consistency with the deep ($\sigma_{850} = 0.25$ mJy) S2CLS COSMOS map (Koprowski et al. 2016) and with previous observations of brighter sources (e.g. Chapman et al. 2005). Fig. 7 indicates the intensity as a function of redshift which is contributed by the galaxies detected in our maps at both wavelengths, this being the result of scaling the redshift distribution to the corresponding intensity. The redshift distribution of the total intensity (stacked plus directly detected sources) is also reported in Table 2 .

As shown in Fig. 7, the redshift distribution of the recovered CIB is different at the two wavelengths, with sources at higher redshifts contributing more at 850 μm. At 450 μm, our results show a peak at $z \sim 1$, in very good agreement with the measurements at 500 μm by Béthermin et al. (2012a), which come from 24 μm catalogues, and with Viero et al. (2013b), who stacked *K*-band-selected sources in *Herschel* maps. Their values have been plotted

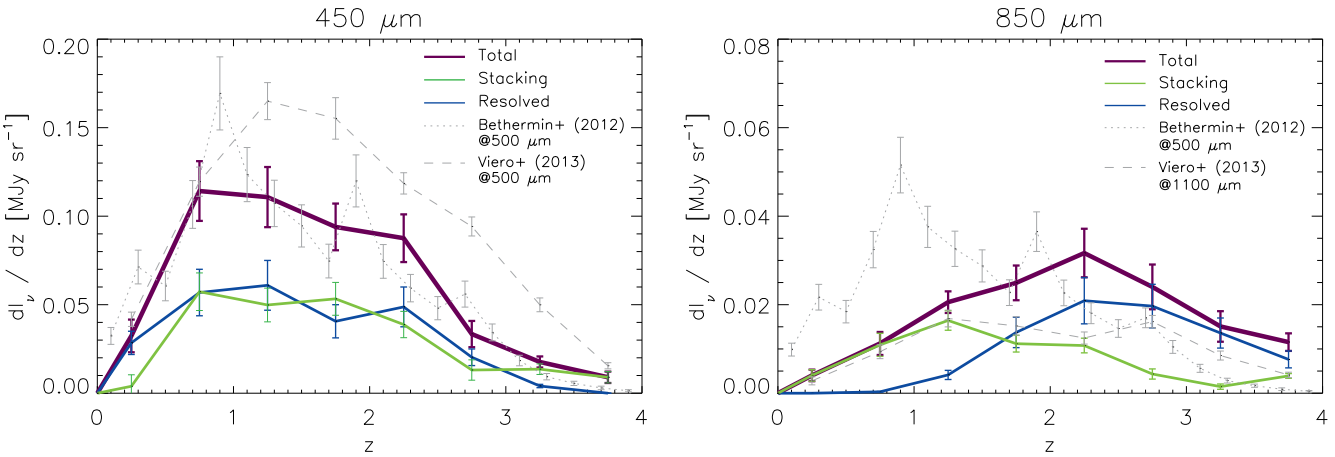

Figure 7. Redshift distributions of the recovered intensity, dI_ν/dz, at 450 μm (left) and 850 μm (right). The blue line represents the contribution of the point sources directly detected in the SCUBA-2 maps and the green line represents the contribution from stacking 24 μm-detected galaxies. The total contribution is plotted as a purple line. For comparison, we plot the results from Béthermin et al. (2012a) at 500 μm and from Viero et al. (2013b) at 500 and 1100 μm. The 500 μm values have been multiplied by a factor of 1.2 and 0.36 to scale their total intensities to match our 450 and 850 μm maps, while the 1100 μm are scaled by 1.75 to match our 850 μm measurements, according to the absolute values measured by Fixsen et al. (1998).

Table 2. Differential recovered intensity as a function of redshift at 450 and 850 μm (as plotted in Fig. 7).

Redshift	450 μm ($\times 10^{-2}$ MJy sr^{-1})	850 μm
$0.0 < z < 0.5$	$3.0^{+1.3}_{-1.1}$	$0.3^{+0.1}_{-0.1}$
$0.5 < z < 1.0$	$12.3^{+2.5}_{-2.0}$	$0.9^{+0.3}_{-0.3}$
$1.0 < z < 1.5$	$12.3^{+2.5}_{-2.0}$	$2.3^{+1.1}_{-0.6}$
$1.5 < z < 2.0$	$9.0^{+1.8}_{-1.5}$	$3.0^{+2.6}_{-1.3}$
$2.0 < z < 2.5$	$9.4^{+2.1}_{-1.6}$	$3.5^{+3.0}_{-1.4}$
$2.5 < z < 3.0$	$4.4^{+1.1}_{-0.9}$	$2.2^{+2.2}_{-1.1}$
$3.0 < z < 3.5$	$1.8^{+0.4}_{-0.4}$	$1.1^{+1.3}_{-0.6}$
$3.5 < z < 4.0$	$1.0^{+0.3}_{-0.3}$	$0.7^{+0.6}_{-0.3}$

in Fig. 7 (left-hand panel) multiplied by a factor of 1.2 to scale the 500 μm estimates to our 450 μm measurements, according to the flux density ratio of the CIB spectrum (Fixsen et al. 1998). At 850 μm, the redshift distribution of the recovered intensity peaks at $z \sim 2$ (see right-hand panel of Fig. 7). We have again plotted the values of Béthermin et al. (2012a, scaled to 850 μm by a factor of 0.36) as a comparison. As shown in this figure, the Béthermin et al. (2012a) redshift distribution is inconsistent with our values, clearly showing that the contribution of higher redshift sources is more important at longer wavelengths. Our estimated redshift distribution is, on the other hand, similar to the one found by Viero et al. (2013b) but at 1100 μm. Their results (scaled at 850 μm by a factor of 1.75) are also plotted in Fig. 7.

Our results highlight that the redshift distribution of the CIB depends on wavelength, with the peak shifting to higher redshifts for longer wavelength bands, and vice versa, as also measured by Marsden et al. (2009), Berta et al. (2011), Béthermin et al. (2012a), and Viero et al. (2013b). This is also consistent with the predictions of different theoretical models of the CIB (e.g. Valiante et al. 2009; Béthermin et al. 2013; Viero et al. 2013a; Mancuso et al. 2016). This selection effect has also been observed in the redshift distributions of SMGs selected at different wavelengths, in which shorter wavelengths select lower z galaxies (and hotter sources), and can be explained with a single population of galaxies (Zavala, Aretxaga & Hughes 2014; Béthermin et al. 2015).

On the other hand, Schmidt et al. (2015), using *Planck* data, have measured a peak at $z \sim 1.2$ for 350, 550 and 850 μm observations, with no obvious wavelength dependence, however, the uncertainties around the peak are large enough to hide or mask out the possible evolution as a function of wavelength, as discussed by these authors.

As discussed above, most of the remaining CIB is expected to be emitted by obscured or low-mass galaxies at $z < 4$ that are not present in the optical/NIR catalogues due to incompleteness, as suggested by the recent work of Viero et al. (2015). However, they also found tentative evidence of higher redshift ($z > 4$) contributions to the CIB at 500 μm. This population of high-z galaxies, which is unreachable with the current optical/NIR surveys (e.g. Kohno et al. 2016), may also contribute to the CIB (although to a lesser extent), especially at longer wavelengths. Actually, Fujimoto et al. (2016) found that the full CIB at 1.2 mm is explained by sources with $S_{1.2} > 0.02$ mJy, but only half of the faintest galaxies ($0.02 < S_{1.2} < 1.2$ mJy) has an optical/NIR counterpart, and none has a radio, suggesting a high-redshift ($z > 3$) nature.

6 SUMMARY

We have presented deep SCUBA-2 observations at 450 and 850 μm in the EGS field as part of the S2CLS. This survey, together with other similarly deep S2CLS maps, represents one of the deepest blank-field observations achieved with single-dish telescopes, reaching a depth of $\sigma_{450} = 1.2$ mJy and $\sigma_{850} = 0.2$ mJy, respectively. Using 57 sources detected above 3.5σ at 450 μm and 90 at 850 μm, we estimate the number counts and the contribution of these galaxies to the CIB.

Our number counts at 450 μm, at a flux density limit of $S_{450} > 4.0$ mJy, are in good agreement with the previous estimation by Geach et al. (2013) derived from S2CLS observations in the COSMOS field. Our result is also consistent with previous shallower observations in blank and gravitational lensed fields.

At 850 μm, our results are the first number counts reported from the deep tier of the S2CLS, and therefore these represent the deepest number counts derived from single-dish blank-field observations using only directly detected sources. Our estimations are in agreement

with the number counts achieved through the benefit of gravitational lensing and with the recent results from interferometric observations with ALMA.

We have also estimated the contribution of the detected sources to the CIB and the contribution of 24 μm-detected galaxies throughout a stacking technique, which give a total of 0.26 ± 0.03 and 0.07 ± 0.01 MJy sr^{-1}, at 450 and 850 μm, respectively, corresponding to 60 ± 20 and 50 ± 20 per cent of the CIB. Using the photometric redshifts available for the 24 μm-detected sample and previously published redshift distributions of the 450 and 850 μm blank-field population, we decompose this emission into bins of redshift, finding an evolution of the redshift distribution of the recovered CIB as a function of wavelength, which peaks at $z \sim 1$ at 450 μm, whereas at 850 μm it peaks at $z \sim 2$, in agreement with theoretical models and previous observations.

The remaining CIB is expected to be emitted by galaxies that are too faint at 24 μm to have been detected in *Spitzer* surveys, as discussed by other authors, although a contribution of high-redshift ($z > 4$) galaxies could also be important, especially at the longer wavelength.

ACKNOWLEDGEMENTS

We would like to thank the referee, Steve Eales, for a helpful report which has improved the clarity of the paper.

This research has been supported by Mexican CONACyT research grant CB-2011-01-167291. JAZ is also supported by a CONACyT studentship. RJI acknowledges support from ERC in the form of the Advanced Investigator Programme, 321302, COSMICISM. The JCMT has historically been operated by the Joint Astronomy Centre on behalf of the Science and Technology Facilities Council of the United Kingdom, the National Research Council of Canada, and the Netherlands Organization for Science Research. Additional funds for the construction of SCUBA-2 were provided by the Canada Foundation for Innovation. This work is based in part on observations made with the *Spitzer Space Telescope*, which is operated by the Jet Propulsion Laboratory, California Institute of Technology under a contract with NASA.

REFERENCES

Aravena M. et al., 2016, A&A, preprint (arXiv:1607.06769)
Austermann J. E. et al., 2009, MNRAS, 393, 1573
Austermann J. E. et al., 2010, MNRAS, 401, 160
Barger A. J., Cowie L. L., Sanders D. B., Fulton E., Taniguchi Y., Sato Y., Kawara K., Okuda H., 1998, Nature, 394, 248
Barro G. et al., 2011a, ApJS, 193, 13
Barro G. et al., 2011b, ApJS, 193, 30
Berta S. et al., 2011, A&A, 532, A49
Béthermin M. et al., 2012a, A&A, 542, A58
Béthermin M. et al., 2012b, ApJ, 757, L23
Béthermin M., Wang L., Doré O., Lagache G., Sargent M., Daddi E., Cousin M., Aussel H., 2013, A&A, 557, A66
Béthermin M., De Breuck C., Sargent M., Daddi E., 2015, A&A, 576, L9
Bintley D. et al., 2014, in Holland W. S., Zmuidzinas J., eds, Millimetre, Submillimetre, and Far-Infrared Detectors and Instrumentation for Astronomy VII. SPIE, Bellingham, p. 915303
Blain A. W., Smail I., Ivison R. J., Kneib J.-P., Frayer D. T., 2002, Phys. Rep., 369, 111
Carniani S. et al., 2015, A&A, 584, A78
Casey C. M. et al., 2013, MNRAS, 436, 1919
Casey C. M., Narayanan D., Cooray A., 2014, Phys. Rep., 541, 45
Chapin E. L. et al., 2011, MNRAS, 411, 505
Chapin E. L., Berry D. S., Gibb A. G., Jenness T., Scott D., Tilanus R. P. J., Economou F., Holland W. S., 2013, MNRAS, 430, 2545
Chapman S. C., Blain A. W., Smail I., Ivison R. J., 2005, ApJ, 622, 772
Chen C.-C., Cowie L. L., Barger A. J., Casey C. M., Lee N., Sanders D. B., Wang W.-H., Williams J. P., 2013, ApJ, 776, 131
Chen C.-C., Cowie L. L., Barger A. J., Wang W.-H., Williams J. P., 2014, ApJ, 789, 12
Chen C.-C. et al., 2016, ApJ, 820, 82
Clements D. L. et al., 2010, A&A, 518, L8
Coppin K., Halpern M., Scott D., Borys C., Chapman S., 2005, MNRAS, 357, 1022
Coppin K. et al., 2006, MNRAS, 372, 1621
Cowie L. L., Barger A. J., Kneib J.-P., 2002, AJ, 123, 2197
Cowley W. I., Lacey C. G., Baugh C. M., Cole S., 2015, MNRAS, 446, 1784
Dempsey J. T. et al., 2013, MNRAS, 430, 2534
Dole H. et al., 2006, A&A, 451, 417
Driver S. P. et al., 2016, ApJ, 827, 108
Dunlop J. S. et al., 2016, MNRAS, preprint (arXiv:1606.00227)
Eales S., Lilly S., Webb T., Dunne L., Gear W., Clements D., Yun M., 2000, AJ, 120, 2244
Fixsen D. J., Dwek E., Mather J. C., Bennett C. L., Shafer R. A., 1998, ApJ, 508, 123
Fujimoto S., Ouchi M., Ono Y., Shibuya T., Ishigaki M., Nagai H., Momose R., 2016, ApJS, 222, 1
Geach J. E. et al., 2013, MNRAS, 432, 53
Geach J. E. et al., 2016, MNRAS, preprint (arXiv:1607.03904)
Glenn J. et al., 2010, MNRAS, 409, 109
Hatsukade B., Ohta K., Seko A., Yabe K., Akiyama M., 2013, ApJ, 769, L27
Hauser M. G. et al., 1998, ApJ, 508, 25
Hayward C. C., Behroozi P. S., Somerville R. S., Primack J. R., Moreno J., Wechsler R. H., 2013, MNRAS, 434, 2572
Heinis S. et al., 2013, MNRAS, 429, 1113
Hodge J. A. et al., 2013, ApJ, 768, 91
Hogg D. W., Turner E. L., 1998, PASP, 110, 727
Holland W. S. et al., 2013, MNRAS, 430, 2513
Hsu L.-Y., Cowie L., Chen C.-C., Barger A., Wang W.-H., 2016, ApJ, 829, 25
Hughes D. H. et al., 1998, Nature, 394, 241
Ivison R. J. et al., 2002, MNRAS, 337, 1
Ivison R. J. et al., 2007a, MNRAS, 380, 199
Ivison R. J. et al., 2007b, ApJ, 660, L77
Jenness T., Berry D., Chapin E., Economou F., Gibb A., Scott D., 2011, in Evans I. N., Accomazzi A., Mink D. J., Rots A. H., eds, ASP Conf. Ser. Vol. 442, Astronomical Data Analysis Software and Systems XX. Astron. Soc. Pac., San Francisco, p. 281
Karim A. et al., 2013, MNRAS, 432, 2
Knudsen K. K., van der Werf P. P., Kneib J.-P., 2008, MNRAS, 384, 1611
Kohno K. et al., 2016, in Kaviraj S., ed., Proc. IAU Symp. 319, Galaxies at High Redshift and Their Evolution Over Cosmic Time. Cambridge Univ. Press, Cambridge, p. 92
Koprowski M. P. et al., 2016, MNRAS, 458, 4321
Kurczynski P., Gawiser E., 2010, AJ, 139, 1592
Lacey C. G. et al., 2016, MNRAS, 462, 3854
Lagache G., Abergel A., Boulanger F., Désert F. X., Puget J.-L., 1999, A&A, 344, 322
Magnelli B. et al., 2013, A&A, 553, A132
Mancuso C., Lapi A., Shi J., Gonzalez-Nuevo J., Aversa R., Danese L., 2016, ApJ, 823, 128
Marsden G. et al., 2009, ApJ, 707, 1729
Oliver S. J. et al., 2010, A&A, 518, L21
Oliver S. J. et al., 2012, MNRAS, 424, 1614
Ono Y., Ouchi M., Kurono Y., Momose R., 2014, ApJ, 795, 5
Oteo I., Zwaan M. A., Ivison R. J., Smail I., Biggs A. D., 2016, ApJ, 822, 36
Patanchon G. et al., 2009, ApJ, 707, 1750
Planck Collaboration XVI, 2014, A&A, 571, A16

Puget J.-L., Abergel A., Bernard J.-P., Boulanger F., Burton W. B., Desert F.-X., Hartmann D., 1996, A&A, 308, L5
Roseboom I. G. et al., 2013, MNRAS, 436, 430
Schmidt S. J., Ménard B., Scranton R., Morrison C. B., Rahman M., Hopkins A. M., 2015, MNRAS, 446, 2696
Scott K. S. et al., 2008, MNRAS, 385, 2225
Scott K. S. et al., 2010, MNRAS, 405, 2260
Serjeant S. et al., 2008, MNRAS, 386, 1907
Simpson J. M. et al., 2015, ApJ, 807, 128
Smail I., Ivison R. J., Blain A. W., 1997, ApJ, 490, L5
Soifer B. T., Neugebauer G., Houck J. R., 1987, ARA&A, 25, 187
Valiante E., Lutz D., Sturm E., Genzel R., Chapin E. L., 2009, ApJ, 701, 1814
Vernstrom T. et al., 2014, MNRAS, 440, 2791
Viero M. P. et al., 2013a, ApJ, 772, 77
Viero M. P. et al., 2013b, ApJ, 779, 32
Viero M. P. et al., 2015, ApJ, 809, L22
Wang W.-H., Cowie L. L., Barger A. J., Williams J. P., 2011, ApJ, 726, L18
Zavala J. A., Aretxaga I., Hughes D. H., 2014, MNRAS, 443, 2384

APPENDIX A: SOURCE CATALOGUES

[1]*Instituto Nacional de Astrofísica, Óptica y Electrónica (INAOE), Luis Enrique Erro 1, Sta. Ma. Tonantzintla, 72840 Puebla, Mexico*

Table A1. EGS/SCUBA-2 450 μm source candidates. The columns give: (1) SCUBA-2 source name, (2) & (3) coordinates, (4) signal-to-noise ratio, (5) measured raw 450 μm flux density and error, (6) deboosted flux density and error estimated through Monte Carlo simulations and (7) deboosted flux density and 68 per cent confidence interval estimated through the Bayesian approach (see Section 3.4).

ID	RA_{450} (hh:mm:ss.s)	$Dec._{450}$ (°:′:″)	S/N_{450}	S_{450} Raw (mJy beam^{-1})	S_{450} Deboosted (mJy beam^{-1})	S_{450} Deebosted (mJy beam^{-1})
S2CLS-EGS-450.01	14:19:42.80	52:50:51.99	11.7	16.2 ± 1.3	16.1 ± 2.1	$15.6^{+1.4}_{-1.2}$
S2CLS-EGS-450.02	14:19:38.82	52:54:01.98	11.6	17.3 ± 1.4	17.0 ± 2.2	$16.6^{+1.4}_{-1.4}$
S2CLS-EGS-450.03	14:19:39.26	52:52:29.98	11.1	14.7 ± 1.3	14.7 ± 2.0	$14.2^{+1.4}_{-1.2}$
S2CLS-EGS-450.04	14:19:41.69	52:52:55.99	10.6	13.5 ± 1.2	13.5 ± 1.9	$13.2^{+1.0}_{-1.4}$
S2CLS-EGS-450.05	14:19:40.14	52:53:25.98	9.9	13.3 ± 1.3	13.3 ± 2.0	$13.0^{+1.2}_{-1.4}$
S2CLS-EGS-450.06	14:19:47.44	52:52:33.99	9.5	11.4 ± 1.1	11.3 ± 1.8	$11.0^{+1.0}_{-1.2}$
S2CLS-EGS-450.07	14:19:20.90	52:55:19.82	9.2	17.5 ± 1.8	17.2 ± 2.9	$16.4^{+2.0}_{-1.6}$
S2CLS-EGS-450.08	14:19:54.72	52:48:39.98	9.2	17.2 ± 1.8	17.0 ± 2.9	$16.6^{+1.6}_{-2.0}$
S2CLS-EGS-450.09	14:19:45.23	52:52:25.99	8.1	9.9 ± 1.2	9.8 ± 1.9	$9.2^{+1.4}_{-1.0}$
S2CLS-EGS-450.10	14:19:30.87	52:52:35.93	7.2	11.4 ± 1.5	11.1 ± 2.4	$10.8^{+1.4}_{-1.6}$
S2CLS-EGS-450.11	14:19:35.96	52:51:07.96	6.5	10.1 ± 1.5	9.7 ± 2.4	$9.4^{+1.4}_{-1.6}$
S2CLS-EGS-450.12	14:19:22.67	52:54:37.84	6.4	11.5 ± 1.7	11.0 ± 2.8	$10.4^{+1.8}_{-1.6}$
S2CLS-EGS-450.13	14:19:53.85	52:54:19.98	6.1	8.8 ± 1.4	8.4 ± 2.2	$8.2^{+1.2}_{-1.6}$
S2CLS-EGS-450.14	14:19:40.81	52:50:25.99	6.1	9.3 ± 1.5	8.8 ± 2.3	$8.4^{+1.6}_{-1.4}$
S2CLS-EGS-450.15	14:20:03.79	52:54:03.92	6.0	10.5 ± 1.7	10.0 ± 2.7	$9.4^{+2.0}_{-1.4}$
S2CLS-EGS-450.16	14:19:58.03	52:51:01.96	5.7	8.7 ± 1.5	8.2 ± 2.3	$8.0^{+1.4}_{-1.6}$
S2CLS-EGS-450.17	14:20:13.31	52:55:31.81	5.6	13.8 ± 2.4	12.9 ± 3.7	$12.4^{+2.0}_{-2.8}$
S2CLS-EGS-450.18	14:19:30.43	52:51:59.92	5.5	8.9 ± 1.6	8.4 ± 2.5	$8.4^{+1.4}_{-1.8}$
S2CLS-EGS-450.19	14:19:40.15	52:49:37.98	5.5	9.6 ± 1.7	8.9 ± 2.7	$8.6^{+1.8}_{-1.6}$
S2CLS-EGS-450.20	14:19:50.97	52:52:11.99	5.4	6.5 ± 1.2	6.2 ± 1.9	$6.0^{+1.2}_{-1.2}$
S2CLS-EGS-450.21	14:19:20.73	52:50:37.81	5.0	10.9 ± 2.1	9.7 ± 3.3	$9.2^{+2.4}_{-2.0}$
S2CLS-EGS-450.22	14:19:30.41	52:55:49.92	4.9	8.9 ± 1.7	7.9 ± 2.9	$7.8^{+1.8}_{-1.8}$
S2CLS-EGS-450.23	14:20:07.78	52:54:59.88	4.9	10.2 ± 2.0	9.1 ± 3.3	$9.2^{+1.8}_{-2.4}$
S2CLS-EGS-450.24	14:19:25.58	52:50:55.87	4.8	9.3 ± 1.9	8.3 ± 3.2	$8.2^{+1.8}_{-2.0}$
S2CLS-EGS-450.25	14:19:47.22	52:54:35.99	4.7	6.6 ± 1.3	6.0 ± 2.2	$6.0^{+1.2}_{-1.6}$
S2CLS-EGS-450.26	14:19:55.17	52:54:07.98	4.7	6.7 ± 1.4	6.1 ± 2.3	$5.8^{+1.6}_{-1.2}$
S2CLS-EGS-450.27	14:19:27.54	52:53:55.90	4.6	8.0 ± 1.7	7.1 ± 2.9	$7.4^{+1.2}_{-2.2}$
S2CLS-EGS-450.28	14:19:47.00	52:53:36.00	4.5	5.6 ± 1.2	5.1 ± 2.0	$5.0^{+1.2}_{-1.2}$
S2CLS-EGS-450.29	14:19:24.47	52:51:57.86	4.5	7.7 ± 1.7	6.6 ± 2.9	$6.4^{+2.0}_{-1.4}$
S2CLS-EGS-450.30	14:19:42.58	52:52:51.99	4.0	5.0 ± 1.2	4.3 ± 2.1	$4.2^{+1.4}_{-1.2}$
S2CLS-EGS-450.31	14:19:33.51	52:53:37.95	4.3	6.9 ± 1.5	5.9 ± 2.6	$6.0^{+1.6}_{-1.6}$
S2CLS-EGS-450.32	14:19:40.15	52:52:27.98	4.9	6.4 ± 1.3	6.0 ± 2.0	$5.8^{+1.2}_{-1.4}$
S2CLS-EGS-450.33	14:20:03.56	52:51:23.92	4.2	7.0 ± 1.6	5.8 ± 2.7	$6.0^{+1.6}_{-1.8}$
S2CLS-EGS-450.34	14:19:52.52	52:55:29.99	4.2	6.7 ± 1.5	5.6 ± 2.6	$6.0^{+1.4}_{-1.8}$
S2CLS-EGS-450.35	14:19:36.84	52:51:45.97	4.2	6.0 ± 1.4	5.2 ± 2.4	$5.0^{+1.6}_{-1.2}$
S2CLS-EGS-450.36	14:19:44.79	52:51:21.99	4.2	5.3 ± 1.2	4.7 ± 2.1	$4.8^{+1.2}_{-1.4}$
S2CLS-EGS-450.37	14:19:59.35	52:48:47.96	4.1	8.0 ± 1.9	6.6 ± 3.2	$6.8^{+1.8}_{-2.2}$
S2CLS-EGS-450.38	14:19:38.83	52:49:31.98	4.1	7.3 ± 1.7	6.0 ± 3.0	$6.2^{+1.8}_{-1.8}$

Table A1 – *continued*

ID	RA_{450} (hh:mm:ss.s)	$Dec._{450}$ (°:′:″)	S/N_{450}	S_{450} Raw (mJy beam^{-1})	S_{450} Deboosted (mJy beam^{-1})	S_{450} Deebosted (mJy beam^{-1})
S2CLS-EGS-450.39	14:19:41.26	52:49:17.99	4.1	7.2 ± 1.7	5.9 ± 2.9	$6.0^{+1.8}_{-1.8}$
S2CLS-EGS-450.40	14:20:09.30	52:51:15.86	4.1	7.7 ± 1.8	6.3 ± 3.1	$6.8^{+1.6}_{-2.2}$
S2CLS-EGS-450.41	14:19:53.19	52:57:27.98	3.9	9.6 ± 2.4	7.3 ± 3.5	$7.4^{+2.8}_{-2.4}$
S2CLS-EGS-450.42	14:19:37.28	52:51:01.97	3.8	5.8 ± 1.5	4.6 ± 2.5	$5.0^{+1.6}_{-1.8}$
S2CLS-EGS-450.43	14:20:05.13	52:55:47.91	3.8	8.0 ± 2.0	6.0 ± 3.4	$6.6^{+2.0}_{-2.4}$
S2CLS-EGS-450.44	14:19:49.20	52:52:33.99	3.8	4.6 ± 1.1	3.8 ± 1.9	$4.0^{+1.2}_{-1.2}$
S2CLS-EGS-450.45	14:19:56.92	52:48:09.97	3.8	7.5 ± 1.9	5.8 ± 3.2	$6.0^{+2.4}_{-2.2}$
S2CLS-EGS-450.46	14:19:25.54	52:55:43.87	3.8	6.9 ± 1.8	5.3 ± 3.0	$5.4^{+2.2}_{-1.8}$
S2CLS-EGS-450.47	14:20:07.97	52:50:39.88	3.8	7.3 ± 1.9	5.6 ± 3.2	$6.0^{+2.2}_{-2.0}$
S2CLS-EGS-450.48	14:19:38.37	52:55:37.98	3.8	6.4 ± 1.6	4.9 ± 2.8	$5.2^{+1.8}_{-1.8}$
S2CLS-EGS-450.49	14:19:17.62	52:52:21.77	3.8	7.8 ± 2.0	6.0 ± 3.3	$6.0^{+2.4}_{-2.0}$
S2CLS-EGS-450.50	14:20:07.99	52:53:45.88	3.7	6.8 ± 1.8	5.1 ± 3.0	$5.4^{+2.2}_{-2.0}$
S2CLS-EGS-450.51	14:19:36.62	52:49:53.97	3.6	6.6 ± 1.8	4.9 ± 2.9	$5.0^{+2.4}_{-1.8}$
S2CLS-EGS-450.52	14:19:47.66	52:50:26.00	3.6	5.2 ± 1.4	4.1 ± 2.3	$4.2^{+1.8}_{-1.4}$
S2CLS-EGS-450.53	14:19:55.16	52:48:47.98	4.3	8.1 ± 1.8	6.8 ± 3.1	$6.6^{+2.2}_{-1.6}$
S2CLS-EGS-450.54	14:20:07.13	52:56:05.89	3.6	8.1 ± 2.2	6.1 ± 3.6	$6.4^{+2.6}_{-3.0}$
S2CLS-EGS-450.55	14:19:41.92	52:48:01.99	3.5	7.2 ± 2.0	5.2 ± 3.1	$5.6^{+2.6}_{-2.4}$
S2CLS-EGS-450.56	14:20:02.00	52:49:37.94	3.5	6.9 ± 1.9	5.0 ± 3.1	$5.0^{+2.8}_{-1.8}$
S2CLS-EGS-450.57	14:20:13.29	52:52:49.81	3.5	6.6 ± 1.8	4.8 ± 2.9	$5.0^{+2.4}_{-2.0}$
S2CLS-EGS-450.58	14:19:50.75	52:54:47.99	3.4	5.0 ± 1.4	3.8 ± 2.2	$4.2^{+1.6}_{-1.8}$
S2CLS-EGS-450.59	14:20:06.41	52:49:15.90	3.4	6.8 ± 1.9	4.8 ± 3.1	$5.4^{+2.2}_{-2.6}$
S2CLS-EGS-450.60	14:19:32.43	52:48:53.94	3.4	7.1 ± 2.0	5.0 ± 3.2	$5.4^{+2.6}_{-2.6}$
S2CLS-EGS-450.61	14:19:49.42	52:51:33.99	3.4	4.3 ± 1.2	3.5 ± 1.9	$3.6^{+1.4}_{-1.4}$
S2CLS-EGS-450.62	14:19:47.22	52:49:58.00	3.4	5.5 ± 1.5	4.0 ± 2.4	$4.2^{+2.0}_{-1.8}$
S2CLS-EGS-450.63	14:19:44.13	52:49:55.99	3.4	5.5 ± 1.6	4.0 ± 2.5	$4.4^{+2.0}_{-2.0}$
S2CLS-EGS-450.64	14:20:12.61	52:51:13.82	3.3	6.3 ± 1.9	4.3 ± 2.9	$5.0^{+2.2}_{-2.6}$
S2CLS-EGS-450.65	14:20:04.45	52:52:51.92	3.3	5.4 ± 1.6	3.8 ± 2.4	$4.4^{+2.0}_{-2.4}$
S2CLS-EGS-450.66	14:19:39.91	52:57:05.98	3.3	6.2 ± 1.8	4.3 ± 2.8	$5.0^{+2.4}_{-2.8}$
S2CLS-EGS-450.67	14:20:08.63	52:50:49.87	3.3	6.3 ± 1.9	4.3 ± 2.9	$5.0^{+2.4}_{-2.8}$
S2CLS-EGS-450.68	14:19:49.65	52:56:47.99	3.2	5.7 ± 1.7	4.0 ± 2.6	$4.2^{+2.6}_{-2.0}$
S2CLS-EGS-450.69	14:19:30.66	52:51:09.93	3.2	5.6 ± 1.7	3.9 ± 2.5	$4.2^{+2.4}_{-2.2}$
S2CLS-EGS-450.70	14:19:37.48	52:55:57.97	3.2	5.6 ± 1.7	3.9 ± 2.5	$4.4^{+2.2}_{-2.8}$
S2CLS-EGS-450.71	14:19:40.81	52:51:59.99	3.2	4.2 ± 1.2	3.2 ± 1.8	$3.4^{+1.6}_{-1.8}$
S2CLS-EGS-450.72	14:19:50.75	52:53:13.99	3.2	3.9 ± 1.2	3.0 ± 1.7	$3.1^{+1.4}_{-1.6}$
S2CLS-EGS-450.73	14:19:48.10	52:56:13.99	3.1	5.2 ± 1.6	3.6 ± 2.4	$4.2^{+2.0}_{-2.8}$
S2CLS-EGS-450.74	14:19:46.77	52:51:46.00	3.1	3.9 ± 1.2	2.9 ± 1.7	$3.2^{+1.4}_{-1.8}$
S2CLS-EGS-450.75	14:19:23.77	52:56:11.85	3.1	7.3 ± 2.2	4.8 ± 3.1	$5.4^{+3.2}_{-5.4}$
S2CLS-EGS-450.76	14:19:18.92	52:54:15.79	3.1	5.9 ± 1.8	4.0 ± 2.7	$4.4^{+2.6}_{-3.0}$
S2CLS-EGS-450.77	14:19:22.68	52:53:37.84	3.1	5.5 ± 1.7	3.8 ± 2.5	$3.6^{+3.0}_{-2.4}$
S2CLS-EGS-450.78	14:19:47.66	52:52:07.99	3.1	3.7 ± 1.2	2.8 ± 1.6	$2.8^{+1.8}_{-1.6}$
S2CLS-EGS-450.79	14:19:49.86	52:49:37.99	3.1	5.2 ± 1.6	3.6 ± 2.4	$4.2^{+2.2}_{-3.0}$
S2CLS-EGS-450.80	14:19:35.27	52:56:53.96	3.1	5.8 ± 1.8	4.0 ± 2.7	$4.4^{+2.6}_{-3.2}$
S2CLS-EGS-450.81	14:19:44.12	52:54:21.99	3.1	4.3 ± 1.3	3.1 ± 1.9	$3.4^{+2.0}_{-2.0}$
S2CLS-EGS-450.82	14:20:09.31	52:52:15.86	3.1	5.4 ± 1.7	3.7 ± 2.4	$4.2^{+2.4}_{-2.8}$
S2CLS-EGS-450.83	14:19:29.74	52:56:49.92	3.1	6.7 ± 2.1	4.4 ± 2.9	$5.0^{+2.8}_{-4.2}$
S2CLS-EGS-450.84	14:19:53.84	52:51:39.98	3.1	4.0 ± 1.2	3.0 ± 1.7	$3.2^{+1.8}_{-2.0}$
S2CLS-EGS-450.85	14:19:57.84	52:56:19.96	3.0	5.6 ± 1.8	3.8 ± 2.6	$4.2^{+2.8}_{-3.6}$
S2CLS-EGS-450.86	14:19:30.41	52:55:17.92	3.0	5.5 ± 1.7	3.7 ± 2.5	$4.0^{+2.6}_{-3.0}$
S2CLS-EGS-450.87	14:20:08.20	52:52:41.88	3.0	5.2 ± 1.7	3.5 ± 2.4	$3.6^{+2.6}_{-3.2}$
S2CLS-EGS-450.88	14:19:29.98	52:53:17.92	3.0	4.9 ± 1.6	3.4 ± 2.3	$3.6^{+2.2}_{-2.8}$
S2CLS-EGS-450.89	14:19:39.93	52:51:05.98	3.0	4.3 ± 1.4	3.1 ± 1.9	$3.4^{+1.8}_{-2.4}$
S2CLS-EGS-450.90	14:20:02.25	52:55:15.93	3.0	5.6 ± 1.8	3.7 ± 2.6	$4.2^{+2.4}_{-3.8}$
S2CLS-EGS-450.91	14:20:15.27	52:51:57.79	3.0	6.0 ± 2.0	3.9 ± 2.7	$4.2^{+3.2}_{-4.2}$
S2CLS-EGS-450.92	14:19:58.05	52:55:13.96	3.0	5.1 ± 1.6	3.4 ± 2.3	$4.2^{+1.8}_{-4.2}$

Table A2. EGS/SCUBA-2 850 μm source candidates. The columns give: (1) SCUBA-2 source name, (2) & (3) coordinates, (4) signal-to-noise ratio, (5) measured raw 850 μm flux density and error, (6) deboosted flux density and error estimated through Monte Carlo simulations and (7) deboosted flux density and 68 per cent confidence interval estimated through the Bayesian approach (see Section 3.4).

ID	RA_{850} (hh:mm:ss.s)	$Dec._{850}$ (°:′:″)	S/N_{850}	S_{850} Raw (mJy beam^{-1})	S_{850} Deboosted (mJy beam^{-1})	S_{850} Deebosted (mJy beam^{-1})
S2CLS-EGS-850.001	14:19:38.82	52:54:01.98	24.2	6.04 ± 0.25	5.96 ± 0.34	$6.0^{+0.2}_{-0.2}$
S2CLS-EGS-850.002	14:19:39.26	52:52:31.98	23.3	5.23 ± 0.22	5.17 ± 0.30	$5.2^{+0.2}_{-0.2}$
S2CLS-EGS-850.003	14:19:40.14	52:53:25.98	23.2	5.30 ± 0.23	5.24 ± 0.31	$5.3^{+0.2}_{-0.2}$
S2CLS-EGS-850.004	14:19:47.66	52:54:37.99	17.0	3.91 ± 0.23	3.87 ± 0.31	$3.8^{+0.3}_{-0.1}$
S2CLS-EGS-850.005	14:19:54.94	52:48:39.98	16.2	5.51 ± 0.34	5.45 ± 0.47	$5.4^{+0.3}_{-0.3}$
S2CLS-EGS-850.006	14:19:54.07	52:54:19.98	16.2	3.70 ± 0.23	3.66 ± 0.31	$3.6^{+0.2}_{-0.2}$
S2CLS-EGS-850.007	14:19:51.19	52:52:11.99	15.0	3.08 ± 0.21	3.05 ± 0.28	$3.0^{+0.2}_{-0.2}$
S2CLS-EGS-850.008	14:20:03.79	52:54:01.92	13.4	3.58 ± 0.27	3.54 ± 0.37	$3.6^{+0.2}_{-0.3}$
S2CLS-EGS-850.009	14:19:22.67	52:54:37.84	12.6	3.82 ± 0.30	3.77 ± 0.41	$3.7^{+0.3}_{-0.2}$
S2CLS-EGS-850.010	14:19:40.81	52:50:27.99	11.8	3.22 ± 0.27	3.20 ± 0.37	$3.2^{+0.2}_{-0.3}$
S2CLS-EGS-850.011	14:19:41.04	52:49:17.99	11.2	3.95 ± 0.35	3.88 ± 0.49	$3.8^{+0.4}_{-0.3}$
S2CLS-EGS-850.012	14:19:47.44	52:52:31.99	11.1	2.24 ± 0.20	2.24 ± 0.27	$2.2^{+0.2}_{-0.2}$
S2CLS-EGS-850.013	14:19:21.34	52:55:21.82	10.8	3.44 ± 0.32	3.41 ± 0.44	$3.4^{+0.3}_{-0.3}$
S2CLS-EGS-850.014	14:19:25.76	52:55:41.88	10.6	3.14 ± 0.30	3.12 ± 0.41	$3.0^{+0.4}_{-0.2}$
S2CLS-EGS-850.015	14:19:45.67	52:52:25.99	8.4	1.73 ± 0.21	1.74 ± 0.29	$1.6^{+0.3}_{-0.1}$
S2CLS-EGS-850.016	14:20:02.00	52:49:37.94	10.4	3.62 ± 0.35	3.56 ± 0.49	$3.6^{+0.2}_{-0.4}$
S2CLS-EGS-850.017	14:19:35.96	52:51:07.96	10.1	2.70 ± 0.27	2.70 ± 0.37	$2.6^{+0.3}_{-0.2}$
S2CLS-EGS-850.018	14:19:54.06	52:51:37.98	10.0	2.19 ± 0.22	2.20 ± 0.30	$2.1^{+0.2}_{-0.2}$
S2CLS-EGS-850.019	14:19:52.97	52:57:27.99	9.6	3.49 ± 0.36	3.43 ± 0.51	$3.4^{+0.3}_{-0.4}$
S2CLS-EGS-850.020	14:20:07.78	52:55:01.88	9.5	2.89 ± 0.31	2.88 ± 0.43	$2.8^{+0.3}_{-0.3}$
S2CLS-EGS-850.021	14:20:12.87	52:55:31.82	9.4	3.13 ± 0.33	3.12 ± 0.47	$2.9^{+0.4}_{-0.2}$
S2CLS-EGS-850.022	14:19:42.80	52:50:51.99	9.2	2.24 ± 0.24	2.24 ± 0.34	$2.1^{+0.3}_{-0.1}$
S2CLS-EGS-850.023	14:20:04.23	52:52:49.92	9.0	2.30 ± 0.26	2.31 ± 0.36	$2.2^{+0.3}_{-0.2}$
S2CLS-EGS-850.024	14:19:41.69	52:52:55.99	9.0	1.95 ± 0.22	1.96 ± 0.30	$1.9^{+0.2}_{-0.2}$
S2CLS-EGS-850.025	14:19:24.47	52:51:57.86	9.0	2.68 ± 0.30	2.68 ± 0.42	$2.6^{+0.3}_{-0.3}$
S2CLS-EGS-850.026	14:19:33.51	52:53:35.95	8.8	2.39 ± 0.27	2.40 ± 0.38	$2.3^{+0.2}_{-0.3}$
S2CLS-EGS-850.027	14:19:38.37	52:56:11.98	8.7	2.24 ± 0.26	2.25 ± 0.36	$2.1^{+0.3}_{-0.2}$
S2CLS-EGS-850.028	14:19:30.44	52:51:07.92	8.2	2.45 ± 0.30	2.45 ± 0.42	$2.3^{+0.3}_{-0.3}$
S2CLS-EGS-850.029	14:19:20.95	52:50:35.82	8.2	3.17 ± 0.39	3.08 ± 0.56	$3.0^{+0.4}_{-0.4}$
S2CLS-EGS-850.030	14:19:30.87	52:52:31.93	8.0	2.14 ± 0.27	2.14 ± 0.38	$2.1^{+0.2}_{-0.3}$
S2CLS-EGS-850.031	14:19:17.62	52:52:21.77	8.0	2.87 ± 0.36	2.82 ± 0.51	$2.8^{+0.3}_{-0.4}$
S2CLS-EGS-850.032	14:19:43.91	52:49:55.99	7.9	2.44 ± 0.31	2.43 ± 0.44	$2.3^{+0.3}_{-0.3}$
S2CLS-EGS-850.033	14:20:06.85	52:49:21.89	7.8	2.72 ± 0.35	2.69 ± 0.50	$2.5^{+0.4}_{-0.3}$
S2CLS-EGS-850.034	14:19:40.13	52:57:03.98	7.5	2.15 ± 0.29	2.14 ± 0.40	$2.1^{+0.2}_{-0.3}$
S2CLS-EGS-850.035	14:19:36.15	52:56:35.96	7.5	2.07 ± 0.28	2.07 ± 0.39	$2.0^{+0.2}_{-0.3}$
S2CLS-EGS-850.036	14:19:37.26	52:55:19.97	7.3	1.89 ± 0.26	1.89 ± 0.36	$1.8^{+0.2}_{-0.3}$
S2CLS-EGS-850.037	14:20:12.17	52:51:11.83	7.3	2.46 ± 0.34	2.45 ± 0.48	$2.3^{+0.3}_{-0.3}$
S2CLS-EGS-850.038	14:19:27.54	52:53:53.90	7.2	2.09 ± 0.29	2.08 ± 0.41	$2.0^{+0.2}_{-0.3}$
S2CLS-EGS-850.039	14:20:09.30	52:51:17.86	7.2	2.36 ± 0.33	2.35 ± 0.47	$2.2^{+0.3}_{-0.3}$
S2CLS-EGS-850.040	14:19:30.41	52:55:49.92	7.1	1.98 ± 0.28	1.97 ± 0.39	$1.9^{+0.2}_{-0.3}$
S2CLS-EGS-850.041	14:19:58.48	52:51:01.96	7.0	1.87 ± 0.27	1.86 ± 0.38	$1.7^{+0.3}_{-0.2}$
S2CLS-EGS-850.042	14:19:55.62	52:54:07.98	4.2	0.96 ± 0.23	0.89 ± 0.32	$0.9^{+0.2}_{-0.2}$
S2CLS-EGS-850.043	14:19:48.10	52:56:15.99	6.9	1.69 ± 0.25	1.68 ± 0.35	$1.6^{+0.2}_{-0.3}$
S2CLS-EGS-850.044	14:20:08.65	52:53:27.87	6.9	1.93 ± 0.28	1.92 ± 0.39	$1.8^{+0.3}_{-0.2}$
S2CLS-EGS-850.045	14:20:3.985	52:48:43.92	6.7	2.39 ± 0.35	2.36 ± 0.50	$2.2^{+0.4}_{-0.3}$
S2CLS-EGS-850.046	14:19:39.27	52:49:33.98	4.6	1.63 ± 0.36	1.50 ± 0.52	$1.3^{+0.4}_{-0.3}$
S2CLS-EGS-850.047	14:19:26.24	52:51:37.88	6.5	1.93 ± 0.30	1.91 ± 0.42	$1.8^{+0.3}_{-0.3}$
S2CLS-EGS-850.048	14:20:11.08	52:53:37.84	6.2	1.82 ± 0.29	1.80 ± 0.41	$1.6^{+0.4}_{-0.2}$
S2CLS-EGS-850.049	14:20:00.26	52:54:01.95	6.0	1.51 ± 0.25	1.49 ± 0.35	$1.3^{+0.3}_{-0.2}$
S2CLS-EGS-850.050	14:19:59.61	52:56:27.95	6.0	1.72 ± 0.29	1.69 ± 0.41	$1.6^{+0.3}_{-0.3}$
S2CLS-EGS-850.051	14:19:58.71	52:54:17.96	4.7	1.17 ± 0.25	1.12 ± 0.35	$1.1^{+0.2}_{-0.2}$
S2CLS-EGS-850.052	14:19:18.92	52:54:15.79	5.8	1.87 ± 0.32	1.83 ± 0.46	$1.7^{+0.3}_{-0.3}$
S2CLS-EGS-850.053	14:19:58.48	52:51:51.96	5.7	1.33 ± 0.23	1.30 ± 0.32	$1.2^{+0.2}_{-0.2}$
S2CLS-EGS-850.054	14:19:29.78	52:50:33.92	5.7	2.01 ± 0.35	1.95 ± 0.51	$1.8^{+0.4}_{-0.3}$

Table A2 – *continued*

ID	RA_{850} (hh:mm:ss.s)	$Dec._{850}$ (°:′:″)	S/N_{850}	S_{850} Raw (mJy beam^{-1})	S_{850} Deboosted (mJy beam^{-1})	S_{850} Deebosted (mJy beam^{-1})
S2CLS-EGS-850.055	14:19:31.30	52:54:43.93	5.6	1.59 ± 0.28	1.56 ± 0.39	$1.3^{+0.4}_{-0.1}$
S2CLS-EGS-850.056	14:20:06.89	52:53:39.89	3.8	1.06 ± 0.28	0.95 ± 0.42	$0.9^{+0.3}_{-0.2}$
S2CLS-EGS-850.057	14:19:59.37	52:53:19.95	5.6	1.29 ± 0.23	1.26 ± 0.32	$1.1^{+0.3}_{-0.1}$
S2CLS-EGS-850.058	14:19:23.59	52:51:07.85	5.6	1.95 ± 0.35	1.89 ± 0.51	$1.7^{+0.4}_{-0.3}$
S2CLS-EGS-850.059	14:19:25.36	52:50:55.87	4.9	1.71 ± 0.35	1.62 ± 0.51	$1.5^{+0.3}_{-0.4}$
S2CLS-EGS-850.060	14:19:23.99	52:56:13.86	5.5	2.20 ± 0.40	2.06 ± 0.57	$2.0^{+0.4}_{-0.4}$
S2CLS-EGS-850.061	14:19:46.55	52:50:06.00	5.4	1.55 ± 0.29	1.51 ± 0.41	$1.3^{+0.3}_{-0.2}$
S2CLS-EGS-850.062	14:20:14.63	52:54:07.79	5.2	1.66 ± 0.32	1.61 ± 0.45	$1.3^{+0.4}_{-0.2}$
S2CLS-EGS-850.063	14:19:27.99	52:52:59.90	5.2	1.45 ± 0.28	1.40 ± 0.39	$1.3^{+0.2}_{-0.3}$
S2CLS-EGS-850.064	14:19:47.22	52:55:27.99	5.2	1.23 ± 0.24	1.19 ± 0.33	$1.1^{+0.2}_{-0.2}$
S2CLS-EGS-850.065	14:19:30.43	52:51:57.92	5.1	1.40 ± 0.27	1.35 ± 0.38	$1.3^{+0.2}_{-0.3}$
S2CLS-EGS-850.066	14:19:45.89	52:48:18.00	5.1	1.86 ± 0.36	1.76 ± 0.52	$1.6^{+0.4}_{-0.3}$
S2CLS-EGS-850.067	14:19:19.37	52:53:35.79	5.1	1.61 ± 0.32	1.55 ± 0.46	$1.3^{+0.4}_{-0.2}$
S2CLS-EGS-850.068	14:19:34.39	52:55:57.95	5.0	1.35 ± 0.27	1.30 ± 0.38	$1.2^{+0.2}_{-0.3}$
S2CLS-EGS-850.069	14:19:49.20	52:52:35.99	3.9	0.80 ± 0.20	0.73 ± 0.30	$0.7^{+0.2}_{-0.2}$
S2CLS-EGS-850.070	14:19:52.30	52:55:31.99	4.9	1.20 ± 0.24	1.15 ± 0.34	$1.1^{+0.2}_{-0.2}$
S2CLS-EGS-850.071	14:19:45.01	52:51:29.99	4.7	1.02 ± 0.22	0.98 ± 0.30	$1.0^{+0.1}_{-0.3}$
S2CLS-EGS-850.072	14:20:03.81	52:56:21.92	4.7	1.41 ± 0.30	1.34 ± 0.43	$1.2^{+0.3}_{-0.2}$
S2CLS-EGS-850.073	14:19:47.44	52:50:26.00	4.5	1.17 ± 0.26	1.11 ± 0.36	$1.1^{+0.2}_{-0.3}$
S2CLS-EGS-850.074	14:19:44.34	52:53:53.99	4.4	0.97 ± 0.22	0.91 ± 0.31	$0.9^{+0.2}_{-0.2}$
S2CLS-EGS-850.075	14:19:20.49	52:52:09.81	4.3	1.37 ± 0.32	1.26 ± 0.46	$1.2^{+0.3}_{-0.3}$
S2CLS-EGS-850.076	14:19:40.13	52:57:19.98	3.3	1.02 ± 0.31	0.83 ± 0.50	$0.9^{+0.3}_{-0.4}$
S2CLS-EGS-850.077	14:20:07.09	52:52:03.89	4.1	1.15 ± 0.28	1.06 ± 0.40	$1.0^{+0.2}_{-0.3}$
S2CLS-EGS-850.078	14:20:08.64	52:52:15.87	3.7	1.06 ± 0.28	0.94 ± 0.43	$1.0^{+0.2}_{-0.3}$
S2CLS-EGS-850.079	14:20:07.13	52:56:09.89	4.1	1.29 ± 0.32	1.17 ± 0.47	$1.0^{+0.4}_{-0.2}$
S2CLS-EGS-850.080	14:19:41.91	52:56:03.99	4.0	0.99 ± 0.25	0.91 ± 0.36	$0.9^{+0.2}_{-0.3}$
S2CLS-EGS-850.081	14:19:49.21	52:53:59.99	4.0	0.86 ± 0.22	0.79 ± 0.32	$0.8^{+0.2}_{-0.2}$
S2CLS-EGS-850.082	14:20:13.29	52:52:57.81	3.9	1.16 ± 0.30	1.04 ± 0.45	$1.0^{+0.3}_{-0.3}$
S2CLS-EGS-850.083	14:19:53.61	52:49:09.98	3.9	1.27 ± 0.33	1.11 ± 0.60	$1.0^{+0.4}_{-0.2}$
S2CLS-EGS-850.084	14:19:51.85	52:49:09.99	3.4	1.09 ± 0.32	0.87 ± 0.54	$1.0^{+0.2}_{-0.5}$
S2CLS-EGS-850.085	14:20:04.00	52:51:25.92	3.9	1.10 ± 0.29	0.98 ± 0.43	$1.0^{+0.2}_{-0.4}$
S2CLS-EGS-850.086	14:19:46.77	52:55:43.99	3.1	0.74 ± 0.24	0.60 ± 0.36	$0.6^{+0.4}_{-0.4}$
S2CLS-EGS-850.087	14:19:44.35	52:49:39.99	3.1	0.99 ± 0.32	0.76 ± 0.52	$0.8^{+0.5}_{-0.4}$
S2CLS-EGS-850.088	14:19:58.93	52:52:39.96	3.7	0.82 ± 0.22	0.72 ± 0.34	$0.8^{+0.1}_{-0.3}$
S2CLS-EGS-850.089	14:20:07.99	52:54:03.88	3.7	1.06 ± 0.29	0.92 ± 0.45	$0.9^{+0.3}_{-0.3}$
S2CLS-EGS-850.090	14:19:41.04	52:48:43.99	3.7	1.35 ± 0.37	1.04 ± 0.79	$1.1^{+0.4}_{-0.4}$
S2CLS-EGS-850.091	14:19:35.96	52:50:17.96	3.6	1.18 ± 0.33	0.94 ± 0.71	$1.0^{+0.3}_{-0.4}$
S2CLS-EGS-850.092	14:19:32.66	52:48:51.94	3.5	1.46 ± 0.41	0.91 ± 0.90	$1.1^{+0.5}_{-0.4}$
S2CLS-EGS-850.093	14:19:43.24	52:55:11.99	3.5	0.85 ± 0.24	0.72 ± 0.38	$0.7^{+0.3}_{-0.2}$
S2CLS-EGS-850.094	14:20:02.89	52:50:29.93	3.5	1.20 ± 0.34	0.93 ± 0.75	$1.0^{+0.3}_{-0.4}$
S2CLS-EGS-850.095	14:19:59.35	52:48:47.96	3.4	1.18 ± 0.35	0.87 ± 0.73	$1.0^{+0.3}_{-0.4}$
S2CLS-EGS-850.096	14:19:44.13	52:49:07.99	3.4	1.16 ± 0.34	0.88 ± 0.73	$1.0^{+0.3}_{-0.4}$
S2CLS-EGS-850.097	14:19:40.59	52:51:57.98	3.4	0.75 ± 0.22	0.64 ± 0.35	$0.6^{+0.3}_{-0.1}$
S2CLS-EGS-850.098	14:19:41.47	52:55:39.99	3.4	0.83 ± 0.25	0.69 ± 0.39	$0.6^{+0.4}_{-0.2}$
S2CLS-EGS-850.099	14:19:46.55	52:56:45.99	3.3	0.87 ± 0.26	0.73 ± 0.41	$0.7^{+0.4}_{-0.2}$
S2CLS-EGS-850.100	14:19:50.75	52:50:49.99	3.3	0.80 ± 0.24	0.66 ± 0.37	$0.6^{+0.4}_{-0.2}$
S2CLS-EGS-850.101	14:19:21.16	52:51:33.82	3.3	1.15 ± 0.35	0.83 ± 0.72	$1.0^{+0.3}_{-0.5}$
S2CLS-EGS-850.102	14:19:30.18	52:56:47.92	3.3	1.05 ± 0.32	0.83 ± 0.53	$0.9^{+0.3}_{-0.4}$
S2CLS-EGS-850.103	14:19:55.38	52:49:53.98	3.3	1.04 ± 0.32	0.82 ± 0.53	$0.9^{+0.4}_{-0.4}$
S2CLS-EGS-850.104	14:19:56.92	52:48:09.97	3.2	1.16 ± 0.36	0.80 ± 0.72	$1.0^{+0.4}_{-0.5}$
S2CLS-EGS-850.105	14:19:34.39	52:54:57.95	3.2	0.86 ± 0.27	0.70 ± 0.42	$0.6^{+0.5}_{-0.2}$
S2CLS-EGS-850.106	14:19:55.83	52:52:59.97	3.2	0.68 ± 0.21	0.56 ± 0.33	$0.6^{+0.3}_{-0.3}$
S2CLS-EGS-850.107	14:20:00.24	52:51:25.95	3.1	0.81 ± 0.26	0.66 ± 0.40	$0.6^{+0.5}_{-0.3}$
S2CLS-EGS-850.108	14:19:27.78	52:52:13.90	3.1	0.85 ± 0.28	0.68 ± 0.43	$0.6^{+0.5}_{-0.4}$

[2]*Center for Astrophysics Research, Science & Technology Research Institute, University of Hertfordshire, Hatfield AL10 9AB, UK*
[3]*H. H. Wills Physics Laboratory, University of Bristol, Tyndall Avenue, Bristol BS8 1TL, UK*
[4]*Herzberg Astronomy and Astrophysics, National Research Council Canada, 5071 West Saanich Road, Victoria, BC V9E 2E7, Canada*
[5]*Department of Physics and Atmospheric Science, Dalhousie University, 6310 Coburg Rd, Halifax, NS B3H 4R2, Canada*
[6]*Department of Physics, Centre for Extragalactic Astronomy, Durham University, South Road, Durham DH1 3LE, UK*
[7]*Astrophysics Group, Imperial College London, Blackett Laboratory, Prince Consort Road, London SW7 2AZ, UK*
[8]*Institute for Astronomy, University of Edinburgh, Royal Observatory, Blackford Hill, Edinburgh EH9 3HJ, UK*
[9]*Department of Physics, Virginia Tech, Blacksburg, VA 24061, USA*
[10]*European Southern Observatory, Karl Schwarzschild Strasse 2, D-85748 Garching, Germany*
[11]*Joint Astronomy Centre, 660 N.A'ohōkū Place, University Park, Hilo, HI 96720, USA*
[12]*Large Synoptic Survey Telescope Project Office, 933 N. Cherry Ave, Tucson, AZ 85721, USA*
[13]*UK Astronomy Technology Centre, Royal Observatory, Blackford Hill, Edinburgh EH9 3HJ, UK*
[14]*Department of Physics & Astronomy, University of British Columbia, 6224 Agricultural Road, Vancouver, BC V6T 1Z1, Canada*
[15]*Kapteyn Astronomical Institute, University of Groningen, Postbus 800, NL-9700 AV Groningen, the Netherlands*
[16]*Leiden Observatory, Leiden University, PO Box 9513, NL-2300 RA Leiden, the Netherlands*

This paper has been typeset from a TEX/LATEX file prepared by the author.